Chapter 5
Drivers and Properties of Waves in the Inner Magnetosphere

How different wave modes are driven, is a central issue in space plasma physics. A practical problem is that often only indirect evidence of the driver can be identified in observations. The plasma environment is complex and variable and already a small difference in background or initial conditions may lead to widely different observable outcomes. In this chapter we discuss drivers of waves causing acceleration, transport and loss of radiation belt particles, whereas Chap. 6 discusses these effects in detail. We note that while this division is motivated in a textbook, it is somewhat artificial and the growth of the waves and their consequences often need to be studied together. For example, a whistler-mode wave can grow from thermal fluctuations due to gyro-resonant interactions until a marginally stable state is reached or nonlinear growth takes over. The growing wave starts to interact with different particle populations leading to damping or further growth of the wave. The fluxes of the higher-energy radiation belt particles are, however, small compared to the lower-energy background population, which supports the wave. Thus their effects on the overall wave activity usually remain small, although the waves can have drastic effect on higher-energy populations. Consequently, these two chapters should be studied together.

Our focus is on the waves that are most relevant to the evolution of radiation belts. A reader interested in a more comprehensive discussion of space plasma waves and instabilities is guided to general textbooks (e.g., Treumann and Baumjohann 1997; Koskinen 2011).

5.1 Growth and Damping of Waves

In Sect. 4.2.2 we found that a small-amplitude electrostatic Langmuir wave in a Maxwellian plasma is attenuated by heating the plasma population. We say that such a plasma is *stable* against *small* perturbations in the particle distribution. To

H. E. J. Koskinen, E. K. J. Kilpua, *Physics of Earth's Radiation Belts*,
Astronomy and Astrophysics Library, https://doi.org/10.1007/978-3-030-82167-8_5

excite a plasma wave in the magnetosphere either an external source, e.g., a VLF transmitter, lightning stroke or an interplanetary shock hitting the magnetopause, or an internal *plasma instability* driven by an unstable particle distribution or magnetic field configuration is required.

To drive plasma unstable the system must contain *free energy* to be transformed to wave energy. The free energy may be stored in the magnetic field configuration such as magnetic tension of a thin current sheet, in an anisotropic plasma pressure, in the streaming of plasma particles with respect to each other, etc. Identification of the free energy source is essential because different sources of free energy can lead to widely different consequences.

The solution to the plasma dispersion equation, $\omega(\mathbf{k}) = \omega_r(\mathbf{k}) + \mathrm{i}\omega_i(\mathbf{k})$, where ω_r is the real part and ω_i the imaginary part of the wave frequency, and $\mathbf{k}$ the wave vector, depends on the local plasma parameters. In radiation belts the plasma conditions vary both spatially and temporally, making the wave environment diverse and complex.

In a stable plasma, the perturbations will eventually be damped ($\omega_i < 0$). For a small damping rate ($|\omega_i| \ll \omega_r$) the perturbation is a normal mode of the plasma. Sometimes the damping is so strong that the oscillation is overdamped. The fluctuation is still there but the wave energy is quickly absorbed by plasma particles. A well-known example of this is the damped ion–acoustic mode in the ionosphere, which determines the spectral shape of the received signal of incoherent scatter radars.

If $\omega_i > 0$, the wave grows and we have an instability. Without doing actual calculations it is impossible to say how large the wave amplitude can grow. This is further complicated by the transport of wave energy from the position where the growth rate is calculated and it is necessary to apply *ray-tracing* to follow the spatial evolution of the wave mode (an example of a widely used ray-tracing procedure is described in detail by Horne 1989). The wave growth in the inner magnetosphere is often limited quasi-linearly by acceleration of particles. The growth may, however, continue to a state where nonlinear effects begin to limit the growth rate. If nothing quenches the growth, the system develops toward a major configurational change, large-scale magnetic reconnection being an important example of such.

5.1.1 Macroscopic Instabilities

Macroscopic instabilities in the configuration space may be intuitively more comprehensible than velocity-space microinstabilities. For example, we can imagine the Earth's magnetic field lines as strings of a huge musical instrument. When an external perturbation hits the system, it tries to restore its original configuration launching a compressional magnetosonic mode, which in turn can excite field-aligned shear Alfvén waves at the eigenfrequencies of the field lines known as *field line resonances* (Sect. 4.4.2).

However, a quantitive description of macroscopic instabilities is far from simple. As stated by Krall and Trivelpiece (1973), "the fluid theory, though of great practical use, relies heavily on the cunning of its user". In collisionless space plasmas the truncation of the moment equations leading, e.g., to magnetohydrodynamics, involves several critical approximations (e.g., Koskinen 2011), which may not be valid under unstable plasma conditions. A well-known phenomenon is the magnetic reconnection, which in the magnetospheric context is an instability of a thin current sheet. In collisionless space plasmas reconnection is often characterized as a tearing of the current sheet in almost ideal MHD. However, the cutting and reconnecting of the macroscopic magnetic field lines is essentially a microscopic process allowing the "de-freezing" of the plasma particles and the magnetic field from each other.

Another example is the MHD version of the hydrodynamic *Kelvin–Helmholtz instability* (KHI) occurring on the magnetopause. The instability is driven by the velocity shear between the faster solar wind flow and the slower flow in the magnetospheric side of the boundary leading to surface oscillations similar to those caused by wind blowing over water. These oscillations may lead to a perturbation that can propagate as an MHD wave into the magnetosphere. The macroscopic process on the magnetospheric boundary requires some type of viscosity similar to the drag in the viscous interaction model of magnetospheric convection proposed by Axford and Hines (1961) already mentioned in Sect. 1.4.1. The viscosity under the plasma conditions at the magnetopause cannot be collisional. Instead it must be provided by wave–particle interactions, thus connecting the macroscopic instability to a microscopic process.

5.1.2 Velocity-Space Instabilities

The discussion of velocity-space instabilities is instructive to start within the linearized Vlasov theory of Sect. 4.2 in the electrostatic approximation. It is an easy exercise to show that in this framework any monotonously decreasing ($\partial f/\partial v < 0$) distribution is stable against small perturbations.

Figure 5.1 is a textbook example of a double-peaked distribution function known as a *gentle-bump distribution*. It consists of a Maxwellian background (density n_1, temperature T_1) and a Maxwellian beam ($n_2,\ T_2$) moving at velocity V_0 with respect to the background. We again consider electrons only and assume that the ions form a cold background. The electron distribution function is now

$$f_{e0} = \frac{n_1}{n_e}\left(\frac{m_e}{2\pi k_B T_1}\right)^{3/2} \exp\left(-\frac{m_e v^2}{2k_B T_1}\right) + \frac{n_2}{n_e}\delta(v_x)\delta(v_y)\left(\frac{m_e}{2\pi k_B T_2}\right)^{1/2} \times \frac{1}{2}\left\{\exp\left(-\frac{m_e(v_z - V_0)^2}{2k_B T_2}\right) + \exp\left(\frac{m_e(v_z + V_0)^2}{2k_B T_2}\right)\right\}. \quad (5.1)$$

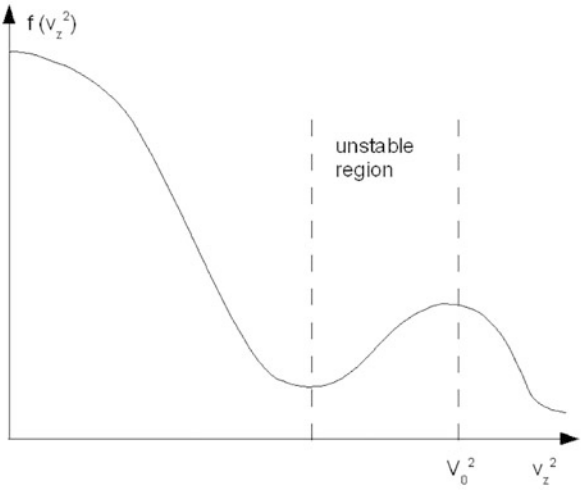

Fig. 5.1 Gentle-bump distribution function with a *potentially* unstable region where $\partial f/\partial v > 0$. In order to avoid a current driven by the bump the electron distribution has been assumed to be symmetric about $v_z = 0$, thus the velocity axis is v_z^2. This way the example remains strictly electrostatic

We further assume that $n_e = n_1 + n_2 \gg n_2$, $T_2 \ll T_1$, $V_0^2 \gg 2k_B T_1/m_e$, i.e., the density and the temperature of the beam are much smaller than those of the background and the beam is faster than the thermal velocity of the background.

In the absence of the bump the solution is the damped Langmuir wave. Now the calculation of $K(\omega, k)$ is somewhat more tedious but still analytically doable applying the same strategy as in Sect. 4.2.2. Due to the "gentleness" of the bump ($n_1 \gg n_2$ and $T_1 \gg T_2$) the real part of the frequency can be approximated by the frequency of the Langmuir wave

$$\omega_r \approx \omega_{pe}(1 + 3k^2\lambda_{De}^2)^{1/2} \approx \omega_{pe}(1 + \frac{3}{2}k^2\lambda_{De}^2) \; . \tag{5.2}$$

The imaginary part is modified from the Landau solution by a term depending on the relative number densities and temperatures of the bump and the background

$$\omega_i \approx -\sqrt{\frac{\pi}{8}}\frac{\omega_{p1}}{|k^3\lambda_{D1}^3|}\exp\left(-\frac{1}{2k^2\lambda_{D1}^2} - \frac{3}{2}\right) + \tag{5.3}$$

$$+ \frac{n_2}{n_1}\left(\frac{T_1}{T_2}\right)^{3/2}\frac{k^3}{k_z^3}\left(\frac{k_z V_0}{\omega_r} - 1\right)\exp\left\{-\frac{T_1/T_2}{2k^2\lambda_{D1}^2}\left(1 - \frac{k_z V_0}{\omega_r}\right)^2\right\} \; .$$

The first term gives the Landau damping caused by the monotonously decreasing background distribution. The second term is stabilizing (damping) to the right from the bump ($v_z > V_0$), where the distribution is decreasing, but it *may* be unstable ($\omega_i > 0$) to plasma oscillations on the ascending slope to the left from the bump. The wave vector of the growing Langmuir wave is close to the direction of the motion of the beam (z-axis), which in magnetized plasmas is typically along the background magnetic field.

The instability requires that the contribution from the positive gradient due to the beam overcomes the damping by the background. This is known as the *gentle-bump* (or *gentle-beam) instability*. If the bump is too gentle, it is not powerful enough to overcome the damping by the background and drive an instability. The only way to find out whether the distribution is stable or unstable is to calculate the imaginary part of the frequency. Recall that even if the wave remains damped ($\omega_i < 0$), the normal mode is there. Its role is to transform kinetic energy of the beam to temperature of the background and beam populations. This gradually leads to filling of the trough between the background and the beam, forming a marginally stable non-Maxwellian distribution.

Two more wave modes, whose growth rate can be found within the electrostatic approximation, are worth of mentioning: the *ion–acoustic wave* (IAC), which is a short-wavelength solution of (4.12), and the *electrostatic ion cyclotron wave* (EIC). They can be driven unstable in a magnetized plasma by a magnetic field-aligned current carried by a field-aligned electron beam, e.g., within and above the auroral region. As these electrostatic modes are of lesser importance in radiation belt physics, we refer to Chap. 7 of Koskinen (2011) for further discussion.

Similarly to the discussion of Landau damping in Sect. 4.2.3, the damping or growth can be illustrated with particles gliding down the slopes of the distribution function and either gaining energy from or losing it to the plasma wave. The instability is enhanced if the number of particles in the bump is increased, if the bump becomes narrower (colder) in the velocity-space, or if the speed of the bump (V_0) increases. In the latter two cases the process approaches the *two-stream instability* of cold plasma theory.

In magnetized space plasmas important unstable distribution functions are loss cone, ion ring, and butterfly distributions (Sect. 3.4), which have positive velocity gradients perpendicular to the magnetic field ($\partial f/\partial v_\perp > 0$). A gyrotropic velocity distribution $f(v_\parallel, v_\perp)$ can also be given as a function of kinetic energy and pitch angle $f(W, \alpha)$, and instabilities can be found if $\partial f/\partial W > 0$ or $\partial f/\partial \alpha > 0$. For example, at the edge of a loss cone the distribution function may have a strong positive gradient $\partial f/\partial \alpha$. Figure 5.2 is a sketch of a potentially unstable butterfly distribution as function of pitch angle. Note further that although an anisotropic bi-Maxwellian pancake distribution has $\partial f/\partial v_\perp < 0$, it can be unstable, because $\partial f/\partial \alpha > 0$. This is a key element of the discussion in Sect. 5.2.

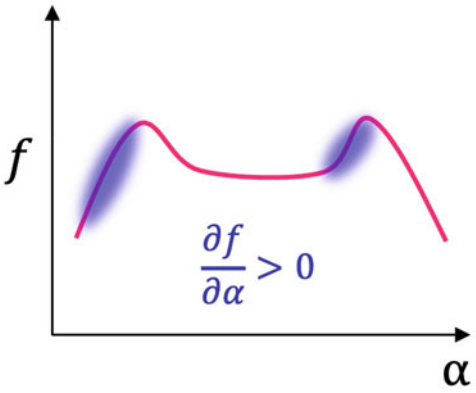

Fig. 5.2 A butterfly distribution function as a function of the pitch angle α, where the shading indicates the potentially unstable ($\partial f/\partial\alpha > 0$) pitch-angle regimes. For a time series of observed flux of butterfly-distributed relativistic electrons, see Fig. 3.4

5.1.3 Resonant Wave–Particle Interactions

To illustrate the resonant interactions between radiation belt particles and electromagnetic plasma waves we investigate the resonance condition (4.38) found from Vlasov theory written in relativistic form as

$$\omega - k_{\parallel} v_{\parallel} = \frac{n\omega_{c\alpha}}{\gamma} \,. \tag{5.4}$$

Here $k_{\parallel}$ can be written as $k\cos\theta$, where θ is the wave normal angle (WNA), i.e. the angle between the background magnetic field and the wave vector, and γ is the Lorentz factor

$$\gamma = (1 - v^2/c^2)^{-1/2} = (1 - v_{\parallel}^2/c^2 - v_{\perp}^2/c^2)^{-1/2}. \tag{5.5}$$

Note that in the relativistic resonance condition the parallel velocity appears both in the Doppler-shift term ($k_{\parallel} v_{\parallel}$) of the wave frequency and in the gyro-frequency term through γ.

In (5.4) n is the order of the Bessel functions in the dielectric tensor of the hot magnetized plasma (4.34) and runs from $-\infty$ to $+\infty$. Thus, both right- and left-hand polarized waves can resonate with both positively and negatively charged particles. $n = 0$ corresponds to the Landau resonance $k_{\parallel} v_{\parallel} = \omega$, whereas $n \neq 0$ give the gyro resonances. Note that for a circularly polarized wave to be in Landau resonance, the wave needs to have a finite WNA because only then the wave has an electric field component parallel to the magnetic field that can accelerate/decelerate the particle. The effect of Landau resonance thus becomes more important the more obliquely the wave propagates.

Equation (5.4) shows that for a gyro resonance to take place the Doppler-shifted frequency of the wave ($\omega - k_{\parallel} v_{\parallel}$) has to match with the particle's gyro frequency $\omega_{c\alpha}/\gamma$ or its higher harmonic. If a particle is mirroring equatorially ($v_{\parallel} = 0$), and/or

the wave propagates purely perpendicular to the background magnetic field ($k_\parallel = 0$), the wave frequency needs to match exactly with the particle's gyro frequency.

The importance of the Doppler shift and the Lorentz factor in fulfilling the resonance condition is obvious when we recall that the frequencies of whistler-mode waves are below, and the frequencies of EMIC waves much below the local electron gyro frequency, which in the outer electron belt is in the range 5–10 kHz. Note that the Lorentz factor of ultra-relativistic electrons is of the order of 5, which alone is not sufficient to shift the frequency to fulfil the resonance condition. Thus both the Doppler shift and the Lorentz factor are essential, in particular, in the interaction of electrons with EMIC waves.

We often need to find the velocities at which radiation belt particles can be in resonance with a wave having a particular frequency and phase speed. Consider waves with a fixed ω and $k_\parallel$ that fulfil the dispersion equation of the wave mode in question. The *resonant velocity* in the non-relativistic case is

$$v_{\parallel,res} = (\omega - n\omega_{c\alpha})/k_\parallel \,. \tag{5.6}$$

Thus the resonance picks up only the velocity component in the parallel direction. The resonance condition does not constrain the perpendicular velocity ($v_\perp$) and the resonant particle can be anywhere on a straight line, called the a *resonant line*, in the ($v_\parallel$, $v_\perp$)-plane, provided that the resonance condition is consistent with the dispersion equation of the wave in question. Resonance is thus possible over a wide range of particle energies.

For relativistic particles (given here for $n = 1$) the gyro-resonant velocity can be solved from

$$v_{\parallel,res} = -\frac{\omega}{k_\parallel}\left(1 - \frac{\omega_{c\alpha}}{\omega}\frac{1}{c}\sqrt{c^2 - v_{\parallel,res}^2 - v_{\perp,res}^2}\right) \tag{5.7}$$

and the parallel and perpendicular velocities are coupled. Instead of a straight resonant line the relativistic resonance condition (5.7) defines a semi-ellipse in the ($v_\parallel$, $v_\perp$)-plane, called a *resonant ellipse*, which constrains the resonant energies. For a wave with a given frequency ω there is now a range of parallel resonant velocities instead of a single $v_{\parallel,res}$ in the nonrelativistic case. Because natural waves in radiation belts have finite frequency bandwidths, there is a finite volume of resonant ellipses in the velocity space. In case of Landau interaction the resonance condition is always $v_{\parallel,res} = \omega/k_\parallel$, and the resonance is independent of $v_\perp$ also in case of relativistic particles.

Let us then consider the effect of several small resonant interactions between the wave and particles, which can lead to damping or amplification of the wave. The combined effect of the interactions is called *diffusion* of the particle distribution in the velocity space.

Kennel and Engelmann (1966) introduced a simple graphical illustration of the diffusion process of non-relativistic particles. Let $\triangle W = \hbar\omega$ be a quantum of energy that a particle gains or loses during a brief interaction with the wave. The change

of parallel momentum can be written as $m\triangle v_\parallel = \hbar k_\parallel$ yielding $\triangle W = m\triangle v_\parallel \omega/k_\parallel$. One the other hand, assuming that the increment of energy from a single interaction is small compared to the total energy of the particle, the change of energy can be expanded as $\triangle W = m(v_\parallel \triangle v_\parallel + v_\perp \triangle v_\perp)$. Equating these two expressions for energy change leads to

$$v_\parallel \triangle v_\parallel + v_\perp \triangle v_\perp = \triangle v_\parallel \, \omega/k_\parallel \,, \tag{5.8}$$

the integral of which is

$$v_\perp^2 + (v_\parallel - \omega/k_\parallel)^2 = \text{constant}\,. \tag{5.9}$$

Equation (5.9) defines circles in the $(v_\perp, v_\parallel)$-plane. The circles are centered at $(0, \omega/k_\parallel)$ and have an increasing radius with increasing $v_\perp$ for a given $v_{\parallel,res}$. For relativistic particles the corresponding equation again defines ellipses (for details, see Summers et al. 1998). These circles (or ellipses) are called *single-wave characteristics*. In Landau resonance the single-wave characteristic is a straight line in the parallel direction.

The resonance occurs when the single-wave characteristic crosses the resonant ellipse, or the straight resonant line in the nonrelativistic case. The characteristic defines the direction of the particle's motion at the time of interaction in the $(v_\perp, v_\parallel)$-plane. In Landau resonance the diffusion is in the $\pm v_\parallel$ direction familiar from the electrostatic Vlasov theory. In gyro resonances the particles move randomly in either direction along the single-wave characteristics and the diffusion is in the direction of the tangent of the single-wave characteristics. The resonant interactions can thus change both the pitch angle and energy of the particles. The net flux of particles is toward the direction of decreasing distribution function along the single-wave characteristics. If the flux is toward increasing energy, as is the case, e.g., with a Maxwellian distribution, the particles gain energy and the wave is damped. In the opposite case, such as for the unstable distributions discussed at the end of Sect. 5.1.2, the wave grows at the expense of particle energy.

Recall again that natural waves in radiation belts have finite frequency bandwidths. Thus there is a family of adjacent single-wave characteristics the particle can resonate with even though it moves away from the single-wave characteristic of the previous interaction. This formulation applies to small-amplitude (linear) waves because $\triangle W$ at each interaction was assumed to be small.[1]

Figure 5.3 illustrates the diffusion due to resonant interaction of electrons with whistler-mode waves in the near-equatorial region of the outer radiation belt. The color-coded distribution function represents an anisotropic population injected from the magnetotail. Due to pitch-angle anisotropy the particles on single-wave

[1] The diffusion along the single-wave characteristics is analogous to the method of characteristics used to solve the Vlasov equation in a magnetized plasma (Sect. 4.2.4). In both cases the changes (either $\triangle W$ or $\triangle f$) at each step are assumed to be small.

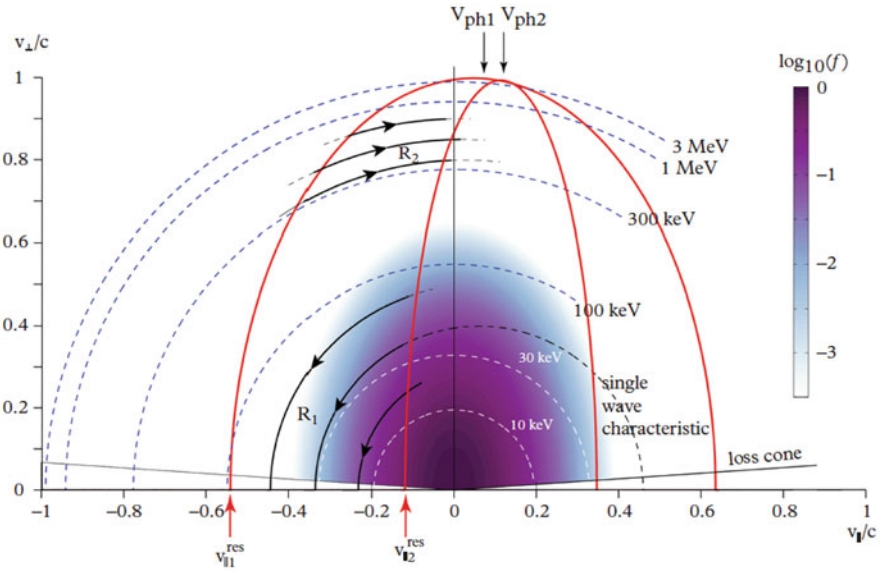

Fig. 5.3 Illustration of resonant ellipses and single-wave characteristics of whistler-mode waves. The dashed lines illustrate constant energy surfaces. The color shading represents a pancake distribution function of thermal/suprathermal electrons. The red lines are resonant ellipses corresponding to 0.1 f_{ce} (the narrower ellipse) and 0.5 f_{ce} (the wider ellipse). The displacement of the ellipses to the right is due to the Doppler shift $k_\parallel v_\parallel$. The black lines are selected single wave characteristics with arrows showing the direction of diffusion. (From Bortnik et al. 2016, reprinted by permission from Oxford University Press)

characteristics labeled R_1 crossing the resonant ellipse, corresponding to resonant velocity $v_{\parallel,2}^{\mathrm{res}}$, diffuse toward smaller pitch angles and lose energy. Thus the whistler-mode wave is amplified as discussed in Sect. 5.2 below. At higher energies ($\gtrsim$ 300 keV), the distribution function is no more anisotropic and the particles on characteristics labeled R_2 diffuse toward larger energies, corresponding to whistler-mode acceleration of radiation belt electrons to be discussed in Sect. 6.4.5.

5.2 Drivers of Whistler-Mode and EMIC Waves

The central role of electromagnetic right-hand polarized whistler-mode waves and left-hand polarized EMIC waves driven by anisotropic velocity distribution functions in the inner magnetosphere was understood already during the 1960s (e.g., Kennel 1966; Kennel and Petschek 1966, and references therein). Those days observations were limited but understanding of plasma theory made it possible to reach results that have later been confirmed using much more extensive and detailed observations.

We discuss below how electron and proton anisotropies drive instabilities generating whistler–mode chorus and EMIC waves in the background inner magnetospheric plasma. Anisotropic electron and proton distributions arise naturally as the particles injected from the magnetotail during substorms move adiabatically toward the stronger magnetic field in the inner magnetosphere. Conservation of the magnetic moment (μ) leads to increase of $W_\perp$ through the drift betatron mechanism. At the same time the bounce paths between northern and southern hemispheres become shorter and the conservation of the longitudinal invariant (J) leads to increase of $W_\parallel$ through Fermi acceleration. In the nearly-dipolar field B is proportional to L^{-3} whereas the length of the bounce motion is proportional to L. Thus in the earthward motion the conservation of μ stretches the distribution function in the perpendicular direction more than the conservation of J in the parallel direction, and the result is a pancake-shaped distribution function ($T_\perp > T_\parallel$).

5.2.1 Anisotropy-Driven Whistler Mode Waves

We follow here the classic presentation of Kennel and Petschek (1966). We begin by considering the cold plasma whistler-mode solution, i.e., the parallel propagating R mode in the frequency range $\omega_{ci} \ll \omega < \omega_{ce}$. In this approximation we can neglect the ion contribution to Eq. (4.62). We are mainly interested in the outer radiation belt domain where electron plasma frequency is larger than the cyclotron frequency (e.g., at $L = 5$ the ratio ω_{pe}/ω_{ce} is about 4). The real part of the frequency can under these conditions be approximated as

$$\frac{c^2 k_\parallel^2}{\omega^2} \approx \frac{\omega_{pe}^2}{\omega(\omega_{ce} - \omega)}. \tag{5.10}$$

To make the discussion simple we consider the interaction with the fundamental ($n = 1$) harmonic of the gyro frequency in non-relativistic approximation ($\gamma = 1$). Inserting (5.10) into the equation of resonant velocity $v_{\parallel,res} = (\omega - \omega_{ce})/k_\parallel$ the *resonant energy* becomes

$$W_{e,res} = \frac{1}{2} m_e v_{\parallel,res}^2 = W_B \frac{\omega_{ce}}{\omega} \left(1 - \frac{\omega}{\omega_{ce}}\right)^3, \tag{5.11}$$

where $W_B = B^2/(2\mu_0 n_0)$ is the magnetic energy per particle, i.e., magnetic energy density divided by particle number density n_0. Note that, as $\omega < \omega_{ce}$, the wave needs to propagate toward the electrons yielding $k_\parallel v_\parallel < 0$ in order the Doppler shift to increase the wave frequency to match with ω_{ce}. In addition, (5.11) implies that the resonant energies are largest at the lowest frequencies and decrease toward zero

when $\omega \to \omega_{ce}$. Under conditions typical in the inner magnetosphere the resonant energies are in the range 1–100 keV.

Let $F_e(v_\parallel, v_\perp)$ be the equilibrium distribution function normalized to 1. With some effort the growth rate of the Vlasov theory solution at the resonant velocity can be written as

$$\omega_i = \pi \omega_{ce} \left(1 - \frac{\omega}{\omega_{ce}}\right)^2 \triangle_e(v_{\parallel,res}) \left(A_e(v_{\parallel,res}) - \frac{1}{(\omega_{ce}/\omega) - 1}\right) \tag{5.12}$$

where

$$\triangle_e(v_{\parallel,res}) = 2\pi \, \frac{\omega_{ce} - \omega}{k_\parallel} \int_0^\infty v_\perp \, \mathrm{d}v_\perp F_e(v_\perp, v_\parallel) \Big|_{v_\parallel = v_{\parallel,res}} \tag{5.13}$$

and

$$\begin{aligned} A_e(v_{\parallel,res}) &= \frac{\displaystyle\int_0^\infty v_\perp \, \mathrm{d}v_\perp \left(v_\parallel \frac{\partial F_e}{\partial v_\perp} - v_\perp \frac{\partial F_e}{\partial v_\parallel}\right) \frac{v_\perp}{v_\parallel}}{\displaystyle 2\int_0^\infty v_\perp \, \mathrm{d}v_\perp F_e} \Big|_{v_\parallel = v_{\parallel,res}} \\ &= \frac{\displaystyle\int_0^\infty v_\perp \, \mathrm{d}v_\perp \tan\alpha \, \frac{\partial F_e}{\partial \alpha}}{\displaystyle 2\int_0^\infty v_\perp \, \mathrm{d}v_\perp F_e} \Big|_{v_\parallel = v_{\parallel,res}} . \end{aligned} \tag{5.14}$$

The factor $\triangle_e(v_{\parallel,res})$ is a measure of the fraction of the total electron distribution close to the resonance. Since $\omega < \omega_{ce}$, $\triangle_e$ is always positive. Recall that while the resonance picks up only one velocity component $v_{\parallel,res}$ in the parallel direction, the electron can have any perpendicular velocity along the resonant line in the $(v_\perp, v_\parallel)$-plane. This motivates the integration over all perpendicular velocities above. If the wave has a wide frequency band, as is the case with naturally occurring whistler-mode waves, a large part of the electron distribution can interact with the wave.

A_e is, in turn, a measure of the anisotropy. It depends on the gradient of F_e with respect to the pitch angle at constant energy. For pancake, loss-cone, and butterfly distributions there are domains of α where $\partial F_e/\partial\alpha > 0$.

Whether ω_i is positive (growing) or negative (damping) depends on the sign of the last term in brackets in the RHS of (5.12). The wave grows when

$$A_e > \frac{1}{(\omega_{ce}/\omega) - 1} \tag{5.15}$$

and attenuates otherwise. This condition can also be expressed in terms of the resonant energy

$$W_{e,res} > \frac{W_B}{A_e(A_e + 1)^2} \, . \tag{5.16}$$

In case of a bi-Maxwellian distribution (3.56) A_e is independent of $v_{\parallel,res}$ and reduces to

$$A_e = \frac{T_\perp - T_\parallel}{T_\parallel}\,. \tag{5.17}$$

Assuming a pancake distribution with $T_\perp > T_\parallel$, which is typically observed in the radiation belt region outside of the plasmapause, the whistler mode grows if the anisotropy is large enough and the condition given by (5.15) or (5.16) is met. The minimum resonant energy can be determined from observations. The more anisotropic the population is, the lower is the minimum resonant energy.

The instability condition for the whistler mode depends on the anisotropy A_e only, but the actual growth or damping rate depends on both A_e and the fraction of resonant electrons $\triangle_e$. Furthermore, (5.15) indicates that the closer to the gyro frequency the wave frequency is, the stronger anisotropy is required to drive the wave due to the increasing resonant damping when $\omega \to \omega_{ce}$.

We have here considered only waves that propagate purely parallel to the background magnetic field. As shown, e.g., by Kennel (1966) the growth rate of the wave decreases with increasing wave normal angle. The generation of oblique whistler-mode waves requires thus gyro resonances occurring for a long enough time. At perpendicular propagation (WNA $\approx$ 90°, i.e., the magnetosonic / X-mode wave) the resonant energy goes to zero. As discussed in Sect. 5.3.2, the magnetosonic mode can be driven unstable by proton ring distributions with free energy in the perpendicular direction ($\partial f/\partial v_\perp > 0$).

5.2.2 *Whistler-Mode Chorus*

The observed whistler-mode waves outside the plasmapause are known as *chorus waves*. They are different from the lightning-generated whistlers with decreasing frequency–time spectra (Sect. 4.3.2). The chorus waves are composed of short, mostly rising, right-hand polarized emissions in the kilohertz range. When played through an audio loudspeaker, the signal resembles a "dawn chorus" of a rookery. According to the appendix of Storey (1953), these dawn choruses had already been heard in the 1930s.

By the early twenty-first century the chorus waves have been demonstrated to be able to accelerate radiation belt electrons to relativistic energies and, on the other hand, to scatter a fraction of the population to the atmospheric loss cone. The acceleration and diffusion processes are dealt in Chap. 6. Here we discuss the main observational features of the waves by walking through Fig. 5.4 reproduced from Bortnik et al. (2016).

The sketch on the top left (Fig. 5.4a) indicates that the chorus emissions are preferentially observed close to the equator outside the plasmasphere from around midnight through the dawn sector to noon. This is consistent with the concept

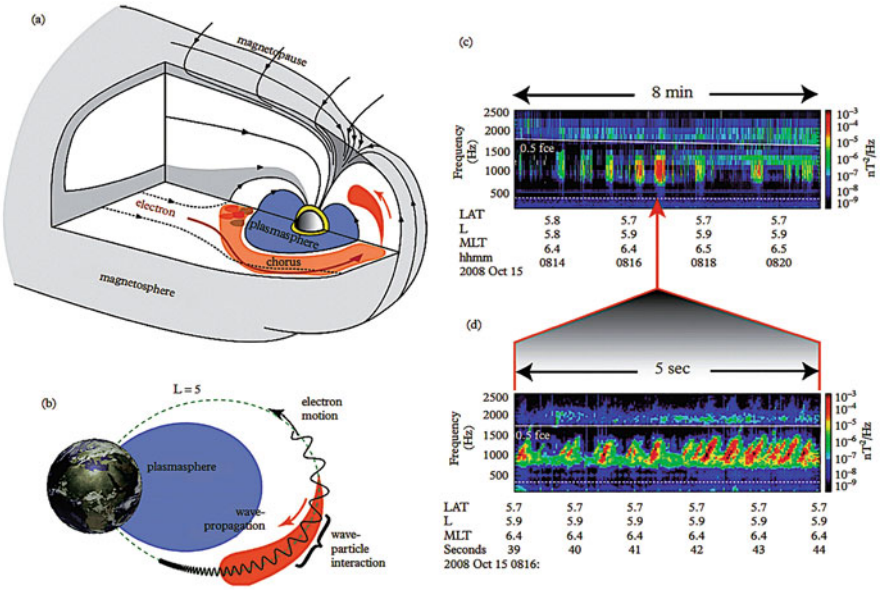

Fig. 5.4 Main observational features of chorus waves. (**a**) The waves appear predominantly close to the equator from midnight through dawn to noon. (**b**) The waves propagate away from the equator, but are attenuated before being reflected from the ionosphere. (**c**) The waves appear as brief bursts in two distinct bands with a cap around 0.5 f_{ce}. (**d**) The individual bursts are composed of short rising tones giving the emissions their chirping characteristics (From Bortnik et al. 2016, reprinted by permission from Oxford University Press)

that they are driven by anisotropic electron populations in the energy range 1–100 keV injected from the magnetotail, since these electrons drift eastward around the plasmapause.

The waves have been found to propagate away from the equator (Fig. 5.4b), but not back to the equator. This suggests that, unlike shear Alfvén waves, the chorus waves do not reflect back from the ionosphere but are attenuated by wave–particle interactions not too far from the equator.

The damping and growth of the waves depend on the wave normal angle. Figure 5.5 based on *Cluster* observations (left) and ray-tracing analysis (right) shows that near the equator the chorus waves propagate parallel or nearly parallel to the background magnetic field, while the obliquity increases with increasing geomagnetic latitude. The generation region close to the equatorial plane can be understood since most of the free energy is concentrated close to the equator, where $\sim$ 90° electrons are trapped and the anisotropy is strongest, which maximizes the gyro-resonant growth of parallel propagating waves. The main attenuation mechanism is likely Landau damping by suprathermal electrons around 1 keV as demonstrated in the ray-tracing study by Bortnik et al. (2007). The attenuation

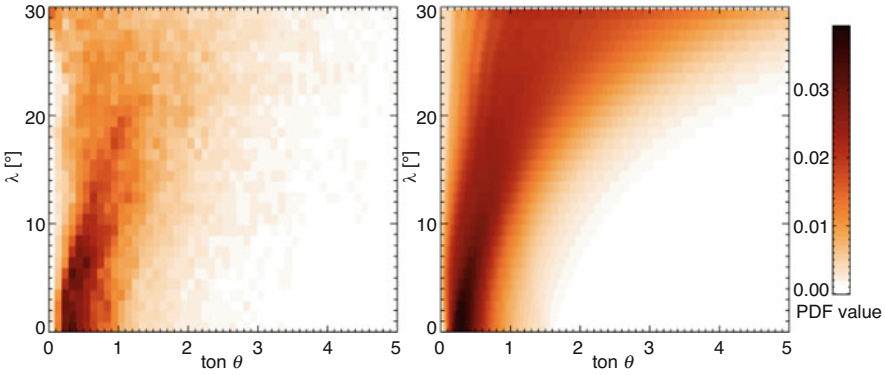

Fig. 5.5 Probability distribution functions (PDF) from *Cluster* observations (left) and three-dimensional ray-tracing (right) of chorus waves as a function of the wave normal angle θ and geomagnetic latitude λ. The observed WNAs are mostly $< 45°$ ($\tan\theta < 1$). (From Breuillard et al. 2012, Creative Commons Attribution 3.0 License)

increases with increasing latitude since the Landau damping is more effective at higher obliquity.

The spectrograms (c) and (d) of Fig. 5.4 illustrate the observed characteristics of the chorus emissions. There are two distinct frequency bands: the lower band in the range $0.1\, f_{ce} < f < 0.5\, f_{ce}$ and the less intense higher-frequency band $0.5\, f_{ce} < f < f_{ce}$. The upper spectrogram indicates that the emissions appear in short bursts of about 10–20 s, whereas the lower spectrogram shows how a single burst is composed of upward chirping signals shorter than a second, which give the chorus-like tone to the emission.

5.2.3 *Two-Band Structure of the Chorus*

The splitting of the chorus emission to two frequency bands (Fig. 5.4) has been a longstanding problem since the OGO 1 and OGO 3 satellite observations during the second half of the 1960s (Burtis and Helliwell 1969, 1976). Several explanations have been proposed ranging from different drivers for each band to nonlinear wave–particle or wave–wave coupling phenomena (see Li et al. 2019, and references therein). The growth of two-band whistler-mode wave with a gap in amplitude at $0.5\, f_{ce}$ has been demonstrated using particle-in-cell plasma simulations assuming the presence of two different anisotropic hot electron distributions (Ratcliffe and Watt 2017), but it is not clear how these two populations would form.

A possible and quite simple scenario to generate electron anisotropy in two distinct energy domains is based on the interplay of the first order gyro resonance $\omega - k_\parallel v_c = \omega_{ce}$ and the Landau resonance $\omega - k_\parallel v_L = 0$, where v_c and v_L represent the gyro- and Landau-resonant parallel velocities. At $\omega = 0.5\,\omega_{ce}$ both conditions

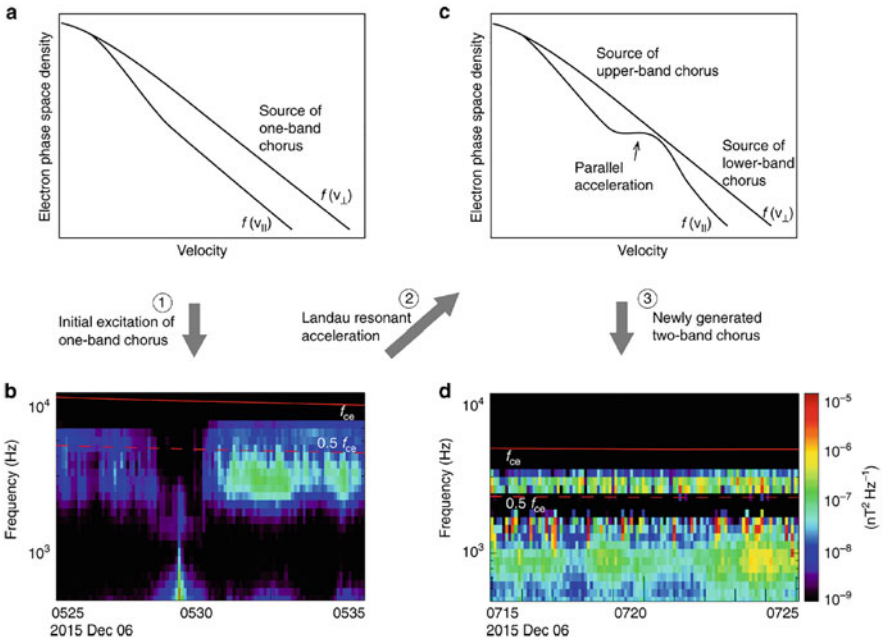

Fig. 5.6 A scenario of the exitation of lower and upper band chorus waves based on Van Allen Probes measurements and numerical simulations. Note that the spectrograms in (**b**) and (**d**) were taken at different periods separated by about 2 hours, when the spacecraft was moving toward a larger distance from the Earth. (From Li et al. 2019, Creative Commons Attribution 4.0 International License)

are fulfilled if v_c and v_L have the same magnitude but are in opposite directions. Thus electrons that should drive the whistler-mode growth actually Landau damp the waves at $\omega = 0.5\,\omega_{ce}$. The damping accelerates electrons in the direction of the background magnetic field reducing the electron anisotropy around the Landau-resonant energy.

Li et al. (2019) studied this mechanism using numerical simulations consistent with *Van Allen Probes* electron and high-resolution wave observations. During the investigated event the electron data indicated two anisotropic electron distributions: one in the range 0.05–2 keV and another > 10 keV. The initial source of free energy in the simulation was an unstable pancake electron distribution injected from the plasma sheet (Fig. 5.6a). First a single-band whistler mode starts growing (Fig. 5.6b) but the Landau damping at $\omega = 0.5\,\omega_{ce}$ quickly sets in and two different anisotropic distributions start forming (Fig. 5.6c). In the simulation the gyro resonance occurred in the energy range 0.22–24 keV, while the Landau-resonant energy was in the range 1.3–2.1 keV. After their formation the two anisotropic populations act separately: the lower energy electrons drive the upper band whistler mode and the upper energy population the lower band (Fig. 5.6d) consistent with the relation of resonant energy and frequency (5.11). Two separate processes are further supported by the common

observation of independent evolution of the upper and lower bands, in particular the different appearance of the rising chirps.

5.2.4 Formation and Nonlinear Growth of the Chirps

The linear theory discussed in Sect. 5.2.1 does not explain the formation of the characteristic rising-tone chirps of the chorus emissions. Their short time scales and large amplitudes point to a nonlinear process.

Omura et al. (2013) reviewed theories and simulations based on nonlinear formation of *electron holes* in phase space. Once an anisotropy-driven coherent wave grows to a finite amplitude, the wave potential around the resonant velocity is able to trap a fraction of the resonant electrons and distort the trajectories of non-trapped resonant electrons. Consequently a hole or a hill forms in the $(\mathbf{r}, \mathbf{v})$ phase space (Fig. 5.7). The deformed electron trajectories correspond to resonant currents that modify the wave field with components: J_E in the direction of the wave electric field and J_B in the direction of the wave magnetic field. It turns out that J_E is responsible for the growth of the wave amplitude whereas J_B leads to the drift in the frequency and the rising tones of the chorus elements. For the detailed calculations we refer to Omura et al. (2013) and references therein.

The continuous filter bank data from the EFW instrument of *Van Allen Probes* has offered the opportunity to reconstruct the frequency and amplitude of large-amplitude whistler-mode waves. Tyler et al. (2019) performed the first statistical analysis based on 5 years of *Van Allen Probes* data. They looked for amplitudes $> 5\ \mathrm{mV\,m^{-1}}$, which are 1–2 orders of magnitude larger than average chorus wave amplitudes. This threshold avoided the risk of contaminating the data set with much smaller-amplitude plasmaspheric hiss emissions. Large-amplitude whistler waves exceeding this level were observed to occur 1–4% of the time from pre-midnight through dawn to noon, mostly between 0–7 MLT, typically above $L = 3.5$. This distribution of the observed wave-packets is consistent with the assumption that they grow from initially anisotropy-driven linear whistler-mode waves.

The nonlinear growth of the chorus elements can continue to very large amplitudes. For example, exceptionally strong electric fields of whistler-mode emissions, about $240\ \mathrm{mV\,m^{-1}}$, were observed by the S/WAVES instruments on the STEREO spacecraft when they passed through the radiation belts on their way to their final orbits (Cattell et al. 2008).

Detailed investigation of the large-amplitude wave packets requires high sampling rate in the time domain and transmission of the waveform to the ground. Thus the relevant observations in any particular region of the magnetosphere have been sparse. Figure 5.8 shows another example of large whistler wave packets in the inner magnetosphere, captured by the Time Domain Sampler onboard the *Wind* spacecraft. The waveform illustrates that the amplitude grows and damps within tens of milliseconds, which makes direct comparisons with local electron data difficult because the particle instruments usually do not have so good time resolution.

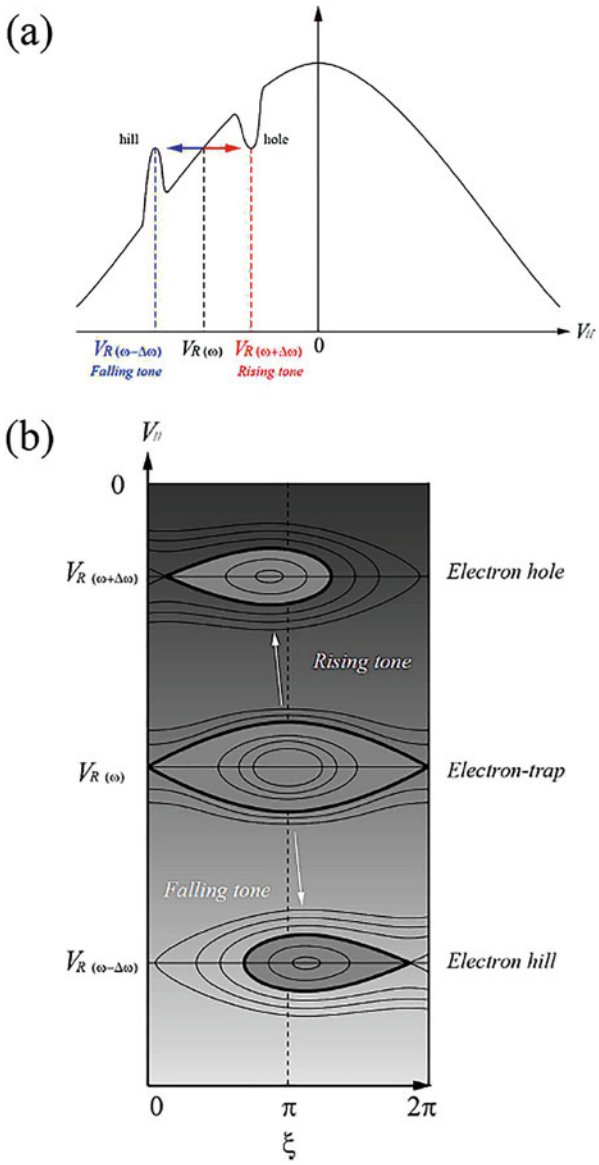

Fig. 5.7 Sketch of the formation of electron holes and hills (**a**) in one-dimensional distribution function $F(v_{\parallel})$ and (**b**) in the phase space $(v_{\parallel}, \xi)$, where ξ is the angle between the perpendicular velocity of a resonant electron and the wave magnetic field (From Omura et al. 2015, reprinted by permission from American Geophysical Union)

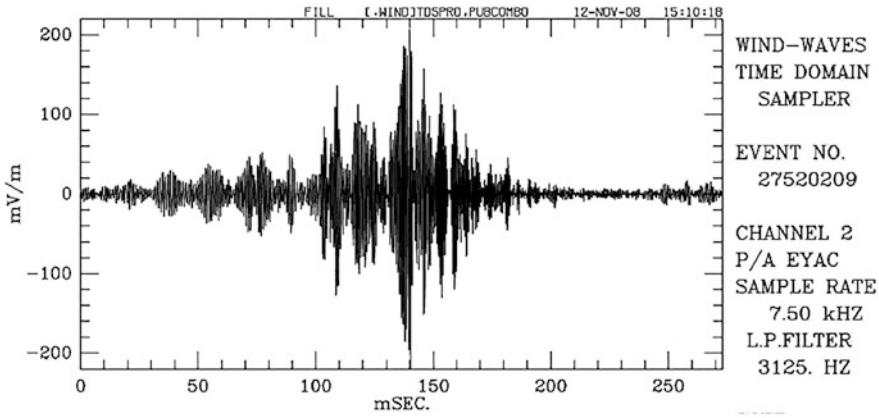

Fig. 5.8 An example of large-amplitude whistler wave packets observed by the Wind spacecraft during its passage through the magnetosphere. (From Kellogg et al. 2011, reprinted by permission from American Geophysical Union)

5.2.5 Spatial Distribution of Chorus Waves

Figure 5.9 shows maps of the average intensity of upper- and lower-band chorus waves compiled from several satellite data sets close to the equator at $L^* \leq 10$ (Meredith et al. 2012, 2020). The low-altitude limit of chorus emissions coincides with the plasmapause and the waves have been observed all the way to the outer rims of the outer belt. As the emissions are driven by anisotropic electrons injected from the plasma sheet during storms and substorms, the occurrence and intensity have strong dependence on magnetospheric activity, which in Fig. 5.9 is represented by the AE index. It is evident that the upper-band chorus waves are limited to a narrower L-range than the lower-band waves. The upper-band emissions also have, on average, significantly smaller peak intensities, typically a few hundred pT^2 compared to lower band chorus with peak intensities of the order of 2000 pT^2.

While chorus waves, in particular the lower-band emissions, are observed at all MLTs, their intensity shows clear MLT-dependence, which becomes more pronounced with increasing geomagnetic activity. The wave occurrence and intensities are strongest from pre-midnight, about 23 MLT, to noon. The database of Meredith et al. (2020) also demonstrates that chorus waves occur considerably more frequently and have larger intensities close to the equator than at higher magnetic latitudes. The trend is particularly clear for the upper-band chorus waves that are rarely detected at higher latitudes. Observations and ray-tracing studies (Bortnik et al. 2007) also show that at the dawn sector chorus waves can propagate to higher latitudes, reaching in the dayside 25°–30°, or above, compared to only 10°–15° in the nightside.

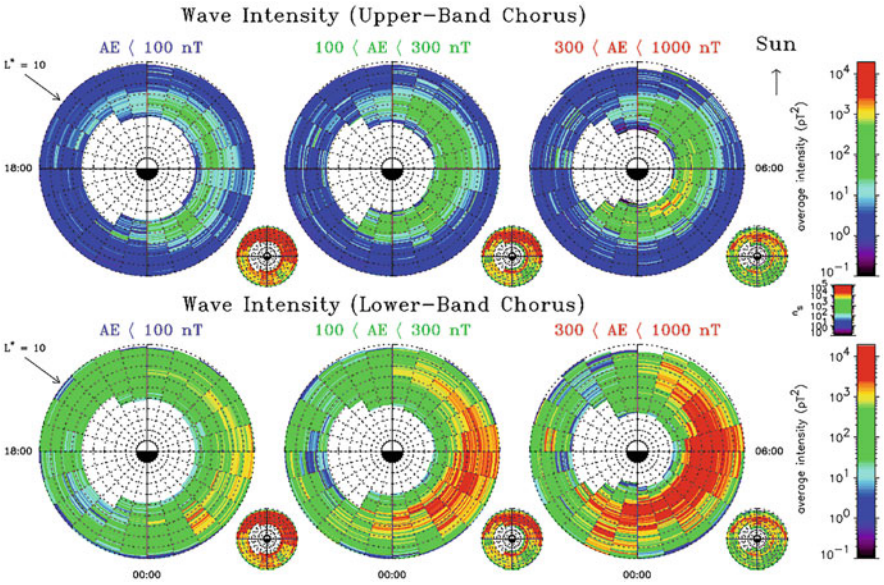

Fig. 5.9 Global maps of the average intensity of upper- and lower-band chorus waves close to the equator $|\lambda_m| < 6°$ as a function L^* and MLT. The small maps show the sampling distributions. The database from which the maps were calculated is a combination of observations from *Dynamics Explorer* 1, CRRES, *Cluster*, *Double Star* TC1, THEMIS and *Van Allen Probes* (From Meredith et al. 2020, reprinted by permission from American Geophysical Union)

These features can be explained by combination of Landau damping by electrons in the keV range and gyro-resonant amplification, which is dominated by tens of keV electrons. The intensification of chorus with geomagnetic activity close to midnight is explained by enhanced substorm injections and strengthening of the earthward convection, both key mechanisms creating the anisotropic electron population to excite chorus waves. The magnetospheric convection also transports the electrons responsible for the Landau damping restricting the propagation of chorus to higher magnetic latitudes. As these electrons drift toward the dayside, they get scattered by wave–particle interactions and the lower-energy electrons scatter faster than higher-energy electrons. As a consequence, closer to noon, chorus waves can propagate to higher latitudes due to smaller amount of Landau-resonant electrons.

A fraction of high-latitude chorus may also be generated locally, e.g., by wave–particle interaction processes with low-energy electrons (from a few hundred eV to a few keV), electron beams or nonlinear wave–wave coupling processes. Furthermore, the scattering of electrons to the atmospheric loss cone, during the drift from midnight toward the noon, can increase the anisotropy and lead to local generation of dayside chorus.

5.2.6 Anisotropy-Driven EMIC Waves

The derivation of the growth rate for left-hand polarized EMIC waves driven by anisotropic ions is similar to that of anisotropic electron-driven whistler-mode waves discussed in Sect. 5.2.1. We start with a single ion species. We focus here on the frequencies close to but below the ion gyro frequency ω_{ci}, which requires an approximation of the dispersion equation different from (5.10)

$$\frac{c^2 k_\parallel^2}{\omega^2} \approx \frac{\omega_{pi}^2}{\omega_{ci}(\omega_{ci} - \omega)}. \tag{5.18}$$

The multiplication by ω_{ci} in the denominator instead of ω as in (5.10) is due to the approximation $\omega \approx \omega_{ci}$. Inserting this again in the expression of resonant velocity, the resonant energy is found to be

$$W_{i,res} = \frac{1}{2} m_i v_{\parallel,res}^2 = W_B \left(\frac{\omega_{ci}}{\omega}\right)^2 \left(1 - \frac{\omega}{\omega_{ci}}\right)^3 \tag{5.19}$$

and the growth rate is

$$\omega_i = \frac{\pi \omega_{ci}}{2} \left(\frac{\omega_{ci}}{\omega}\right) \frac{(1 - \omega/\omega_{ci})^2}{(1 - \omega/(2\omega_{ci}))} \triangle_i(v_{\parallel,res}) \left(A_i(v_{\parallel,res}) - \frac{1}{(\omega_{ci}/\omega) - 1}\right), \tag{5.20}$$

where $\triangle_i$ and A_i are defined in the same way as in Sect. 5.2.1. The main difference to the electron case is the narrower frequency range close to the ion gyro frequency where the ions can cause significant wave growth. The threshold resonant energy for the EMIC wave is

$$W_{i,res} > \frac{W_B}{A_i^2(A_i + 1)}. \tag{5.21}$$

In the inner magnetosphere the frequencies of the chorus waves are a few kHz and of EMIC waves $\lesssim$ 1 Hz. Once generated by the anisotropic suprathermal anisotropic electrons the chorus waves can be in resonance with radiation belt electrons of energies $\gtrsim$ 30 keV, whereas gyro-resonant interaction of electrons with EMIC waves requires MeV energies. These interactions can lead to both damping or further growth of the waves depending on the actual shape of the distribution function of the high-energy population as discussed in Chap. 6.

5.2.7 *Multiple-Ion Species and EMIC Waves*

The inner magnetospheric plasma contains a variable mixture of protons and He^+ and O^+ ions. The multi-ion dispersion equation has resonances at the gyro frequencies of each species. Consequently, the EMIC waves appear in separate frequency bands: Hydrogen band emission occurs between helium and proton gyro frequencies and the helium band between oxygen and helium gyro frequencies (Fig. 4.5). Sometimes an oxygen band below the oxygen gyro frequency is also observed.

The presence of cold ions of ionospheric origin lowers the threshold for the excitation of EMIC waves and enhances the wave growth. Cold ions are indeed sometimes referred to as "generation catalyst" for EMIC waves (Young et al. 1981). EMIC waves are excited in the regions of minimum magnetic field of a given magnetic flux tube close to the equator, where the hot anisotropic ions are concentrated. After generation the waves propagate along the magnetic field toward the increasing field. Ray-tracing studies further show that the growth rates of EMIC waves are considerably larger outside than inside the plasmasphere.

Keika et al. (2013) conducted a comprehensive statistical analysis of EMIC wave observations by AMPTE/CCE from years 1984–1989. As shown in Fig. 5.10, EMIC waves were observed mostly beyond $L = 4$ at all local times and preferentially in the noon–afternoon sector beyond $L = 6$. Similar results were obtained by Meredith et al. (2003) using CRRES observations and by Chen et al. (2019) who analyzed 64 months of *Van Allen Probes* observations, the latter of which do not reach as far out as AMPTE/CCE but allow for more detailed analysis of wave properties.

Keika et al. (2013) found that, similar to chorus waves, the MLT distribution of EMIC waves depends on geomagnetic activity. During quiet times EMIC waves are distributed more symmetrically and their occurrence peaks close to noon. During geomagnetically active conditions the occurrence is most frequent near noon and in the dusk sector, where waves in the He^+ band have the strongest concentration. The plasmaspheric plume with cold ions at afternoon hours (Sect. 1.3.2) overlaps with the region of anisotropic hotter ring current ions. In other words, in the afternoon

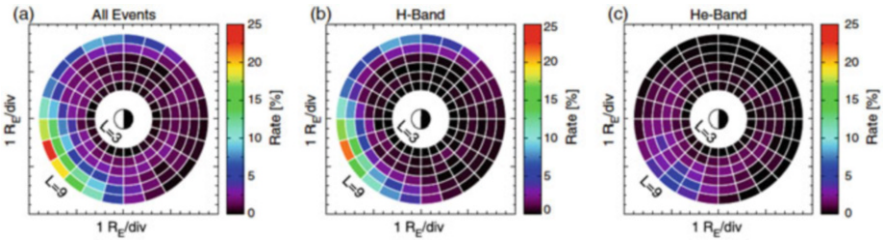

Fig. 5.10 Occurrence rates of all EMIC wave events (left), hydrogen band events (middle) and helium band events during 4.5 years of AMPTE/CCE data. Note that different to Fig. 5.9 noon is to the left. (From Keika et al. 2013, reprinted by permission from American Geophysical Union)

sector hot and cold ion populations coexist. The hot population provides free energy to excite the waves and the cold population enhances the growth. The amplitude of EMIC waves also increases with geomagnetic activity and shows a similar MLT trend as the occurrence rate. The wave amplitudes are strongest in the He^+ band.

Based on their statistical results Keika et al. (2013) suggested that the helium band would be more sensitive to ion injections, whereas the hydrogen band would benefit from solar wind compression of the magnetosphere. The compression enhances drift shell splitting and formation of Shabansky orbits (Sect. 2.6.2), which both can lead to temperature anisotropy ($T_\perp > T_\parallel$) and drive EMIC waves locally on the dayside (e.g., Usanova and Mann 2016, and references therein).

5.3 Plasmaspheric Hiss and Magnetosonic Noise

Inside the plasmasphere the main wave modes affecting electron dynamics are *plasmaspheric hiss* and *equatorial magnetosonic noise*. Hiss is of key importance to scattering electrons to the atmospheric loss cone at wide range of energies and forming the slot region, while magnetosonic waves can resonate with energetic electrons and transfer energy from ring current protons to radiation belt electrons. While the hiss is confined within the plasmasphere, the magnetosonic noise can occur both inside and outside the plasmapause.

5.3.1 Driving of Plasmaspheric Hiss

The plasmaspheric hiss is a whistler-mode emission that derives its name from the early observations of structureless spectral properties that resemble audible hiss found at all magnetic local times in the plasmasphere (Thorne et al. 1973). The frequencies of the emissions extend from a few tens of Hz to a few kHz, which is well below the local electron gyro frequency of more than 10 kHz. The high time-resolution observations with the EMFISIS instrument of the *Van Allen Probes* (Summers et al. 2014) have, however, shown that the hiss is not quite as structureless as previously thought but contains quasi-coherent rising and descending tones similar to the whistler-mode chorus wave packets outside the plasmapause (Sect. 5.2.2).

Figure 5.11 shows the distribution of plasmaspheric hiss based on more than two years of *Van Allen Probes* data. Hiss occurs at all MLTs, but the amplitudes are clearly largest on the dayside. The wave amplitudes on the dayside also increase considerably with the level of geomagnetic activity. During geomagnetically quiet periods the amplitudes range from a few pT to a few tens of pT, whereas during magnetic storms the amplitudes increase to 100–300 pT. Figure 5.11 also demonstrates that hiss waves propagate predominantly parallel to the magnetic field at low magnetic latitudes becoming more oblique at higher latitudes.

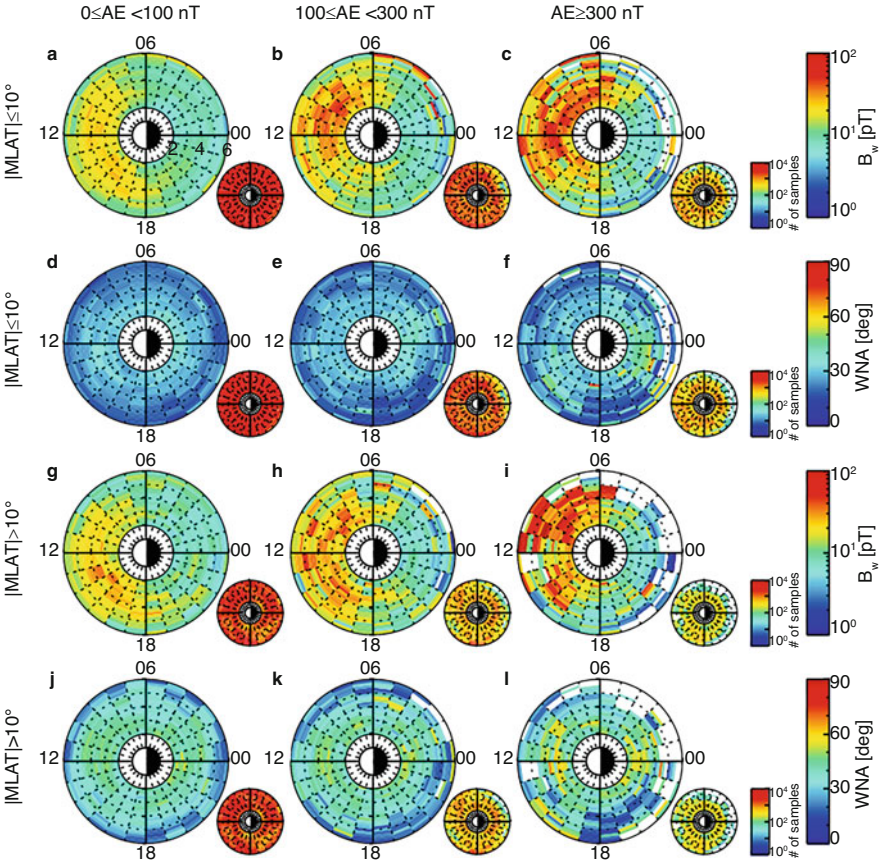

Fig. 5.11 Distribution of hiss amplitude and wave normal angles as observed by *Van Allen Probes* in the range from 10 Hz to 12 kHz for different geomagnetic activity conditions in terms of the *AE* index. The uppermost row indicates the median wave magnetic field amplitude in picoteslas and the second row the median wave normal angle at magnetic latitudes close to the equator ($\lambda \leq 10°$). The third and fourth rows are the corresponding quantities at higher magnetic latitudes. The small maps give the distribution of the samples in each picture. (From Yu et al. 2017, reprinted by permission from American Geophysical Union)

The origin of plasmaspheric hiss remains unclear. Suggested generation mechanisms include triggering through terrestrial lightning strikes, local generation within the plasmasphere, and penetration of chorus waves into the plasmasphere.

The occurrence and geographic distribution of the higher-frequency part of hiss (1–5 kHz) correlate with lightning strikes (Meredith et al. 2006), while at lower frequencies (0.1–1 kHz) no such correlation has been found. Furthermore, lightning is not related to magnetospheric activity whereas plasmaspheric hiss is. The wave power of the higher-frequency hiss is about an order of magnitude smaller than the

power of the lower-frequency hiss. Consequently, lightning-induced hiss emissions likely are of minor importance to radiation belt dynamics.

Because early ray-tracing studies had indicated that there could be no significant penetration of whistler-mode chorus waves through the plasmapause, Thorne et al. (1973) advocated local generation through a similar gyro-resonant instability as the growth of whistler-mode emissions outside the plasmapause (Sect. 5.2.1). However, the anisotropic suprathermal plasma does not penetrate to the plasmasphere and later studies have shown that the linear growth rates remain small in the plasmasphere.

While the linear growth seems less likely, the high-resolution vector waveform samples of the *Van Allen Probes* EMFISIS observations (Fig. 5.12) have revealed that hiss features complex quasi-coherent fine-structures with discrete rising and falling tones. The spectral intensities peak at lowest frequencies, decreasing in amplitude with increasing frequency. The structures resemble the chirps of the whistler-mode chorus emissions outside the plasmapause, but they persist only a few milliseconds, which corresponds to about 10 wave periods, whereas the timescale of chorus chirps is of the order of 100 wave periods.

The quasi-coherent structures may be explainable by a similar nonlinear growth mechanism as was discussed in the context of chorus wave chirps in Sect. 5.2.4 (Omura et al. 2015; Nakamura et al. 2016). When a critical wave amplitude is exceeded due to resonant electrons' interaction with the waves, electron hills and holes form in the velocity space (Fig. 5.7), which give rise to falling and rising tones. The different coherent tones in hiss correspond to waves at different frequencies associated with different resonant velocities. The seed waves subject to nonlinear growth could originate from any of the sources mentioned above or from local thermal fluctuations. Since the nonlinear growth rate is much larger than the linear, local generation of hiss in the plasmasphere may be a viable option.

The observations of hiss fine structure do not preclude the chorus–hiss connection, of which there is circumstantial evidence in satellite observations (e.g., Santolík et al. 2006; Bortnik et al. 2008b, and references therein). The hypothesis of chorus wave penetration was revived by ray-tracing studies of Bortnik et al. (2008b). Figure 5.13 illustrates an example of tracing of waves launched at $L = 5$ at the equator in the lower end of the chorus frequency range. The initial wave normal angles extended from $-70°$ to $+20°$ with negative angles corresponding to earthward inclination. The waves with negative WNAs of a few tens of degrees on the nightside were found to be able to penetrate to the plasmasphere, while on the dayside this may occur over a wider range of WNAs, from approximately $-60°$ to $-30°$. This is due to significantly smaller dayside fluxes of about 1 keV-electrons that would Landau-damp the waves. Inside the plasmasphere the waves reflect at higher latitudes ($\lambda \approx 30$–$40°$) closer to the Earth, where their frequency becomes less than the local cut-off frequency.

The chorus waves have specific entry points into the plasmasphere but they become quickly randomized after a few cycles of reflections. This is consistent with the unstructured appearance of hiss in low-resolution observations as illustrated in the bottom panels of Fig. 5.13. The figure also shows that chorus waves outside the plasmapause have larger wave power than hiss in the plasmasphere.

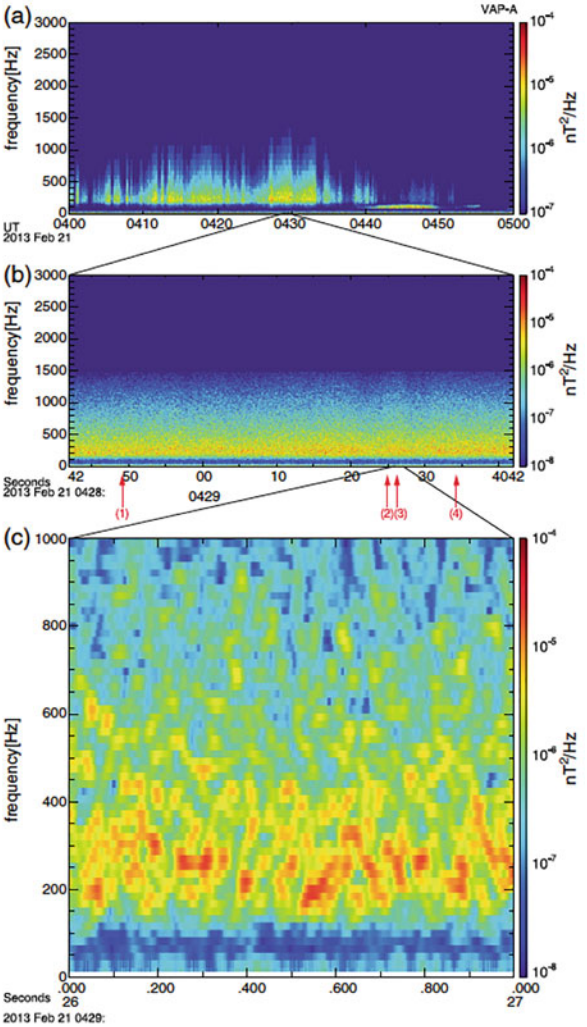

Fig. 5.12 An example of plasmaspheric hiss consisting of coherent rising and falling tones (From Summers et al. 2014, reprinted by permission from American Geophysical Union)

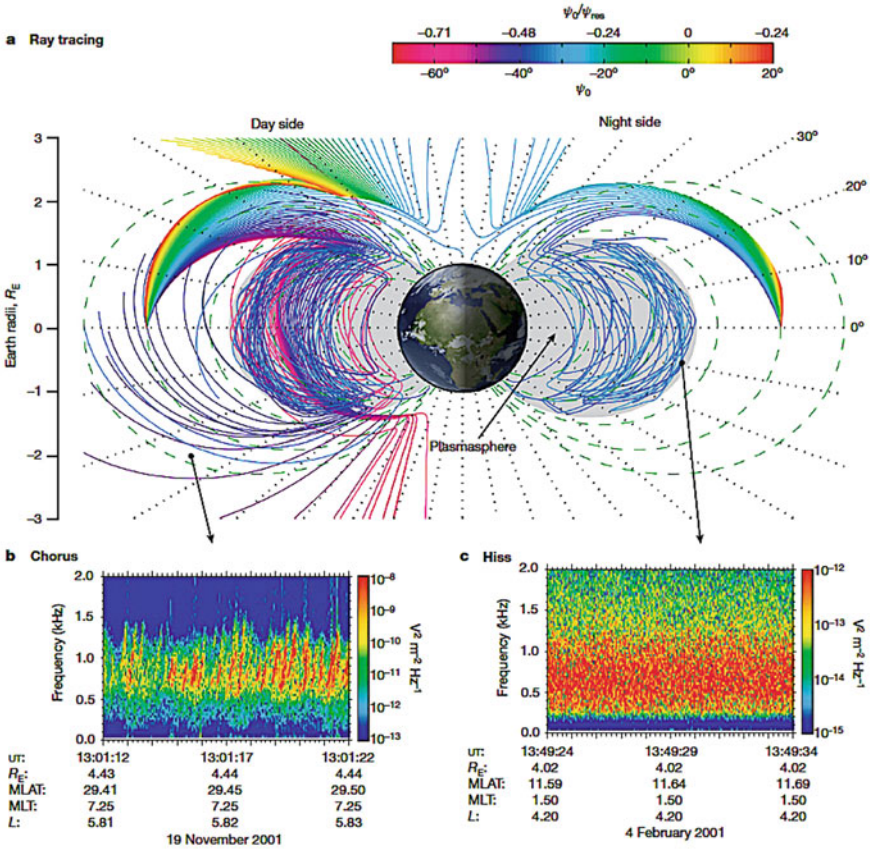

Fig. 5.13 (**a**) Ray-tracing results of chorus waves launched from the equator with different wave normal angles ψ_0 (negative values correspond to earthward propagation) at 0.1 f_{ce}. Bottom panels show the typical examples of intensities of (**b**) chorus on the dayside outside the plasmasphere and (**c**) hiss on the nightside inside the plasmasphere from *Cluster* observations. (From Bortnik et al. 2008b, reprinted by permission from SpringerNature)

Once the waves have penetrated to the plasmasphere, they refract from the large density gradient at the plasmapause and become trapped inside the plasmasphere. In contrast to chorus waves outside the plasmapause, Landau damping of the hiss waves in the plasmasphere is weak due to the high number density of cold electrons and small flux of Landau-resonant electrons. The waves can thus propagate over long time periods passing repeatedly through the equatorial region. The waves become more field-aligned, as they approach the equator, where they can get gradually amplified by gyro resonance with electrons.

The day–night asymmetry of hiss amplitudes (Fig. 5.11) agrees with the ray-tracing results and the chorus penetration hypothesis as the origin of hiss. This is also consistent with hiss intensifying with geomagnetic activity, similarly to chorus

waves. Furthermore, the compression of the dayside magnetosphere creates local magnetic field minima away from the equator (Fig. 2.9) where the growth rate of chorus waves increases and from where they have a shorter distance to propagate to the plasmapause, minimizing the Landau damping before entering the plasmasphere (Tsurutani et al. 2019).

The penetration of chorus waves through the plasmapause depends on both the WNA and the inclination of the wave vector, of which the latter must naturally be toward the Earth. Using *Van Allen Probes* EMFISIS data Hartley et al. (2019) investigated how often the observed wave vectors of chorus emissions are in favorable direction for penetration. They found that the inclination is actually predominantly oriented in the anti-earthward direction. Their ray-tracing computations indicated that only a very small fraction of wave power, typically less than 1%, would propagate to the plasmasphere. The only exception were waves that were emitted very close to the morning sector plasmaspheric plume, located in their model at $L = 5$ and MLT = 14. In the plume region about 90% of the lower-band chorus power was found to propagate into the plasmasphere. In another study Kim and Shprits (2019) showed, based on four years of *Van Allen Probes* observations, that similar to hiss in the plasmasphere proper, the hiss in the plume has amplitudes from a few pT to more than 100 pT. In fact, the plume may provide an efficient entrance for the hiss to penetrate to the plasmasphere, but whether it is enough, remains unclear.

Further indication of chorus–hiss connection was found by Agapitov et al. (2018) in an extensive correlation analysis of THEMIS observations of lower-band chorus and hiss waves during 2007–2017 at times when one of the spacecraft was in the plasmasphere and another outside the plasmapause. They considered 2-min intervals of events where the wave amplitude was required to be larger than 1 pT and the distance between the spacecraft more than $2\,R_E$ but less than 3 h in MLT. The correlations were calculated when chorus waves were observed within 10 s before hiss or hiss during 10 s following the chorus observation. They found 71,000 time intervals when the correlation coefficient between chorus and hiss wave power dynamics was larger than 0.5, often larger than 0.7. The best correlations were in the noon to afternoon sector consistent with favorable penetration of chorus waves to the plasmasphere in the sector of the plasmaspheric plume. Even if the amount of penetrating wave energy may be small, Agapitov et al. (2018) argued that it may form an embryonic source for local amplification by, e.g., the above mentioned nonlinear mechanism.

5.3.2 Equatorial Magnetosonic Noise

Perpendicular propagating waves in the frequency range between the proton gyro frequency (ω_{cp}) and the lower hybrid resonance frequency ($\omega_{LHR} \approx \sqrt{\omega_{ce}\omega_{cp}}$) confined within a few degrees from the Earth's magnetic equator were first identified in the OGO 3 satellite observations and were named *equatorial noise* (Russell et al.

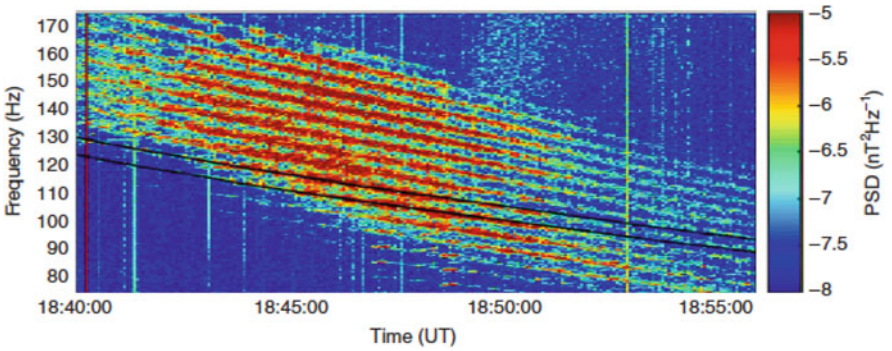

Fig. 5.14 Example of fine-structured magnetosonic waves from *Cluster* observations. The frequency bands are separated by the local proton gyro frequency. The descending trend if the stripes is due to the motion of the spacecraft in the direction of decreasing magnetic field (From Balikhin et al. 2015, Creative Commons Attribution 4.0 International License)

1970). This emission features distinct bands of ion Bernstein modes organized by multiples of the proton gyro frequency (Fig. 5.14). The wave mode is the hot plasma equivalent of the linearly polarized cold plasma X-mode that propagates almost perpendicular (WNA $\approx 89°$) to the background magnetic field. The mode is an extension of the MHD fast magnetosonic mode above ω_{cp} (Fig. 4.6) and the observed emission is commonly called *equatorial magnetosonic noise*. While these waves evidently are related to ion dynamics, they are also of significant interest for radiation belt electrons, as they can resonate with energetic electrons through Landau, gyro and bounce resonances as discussed in Chap. 6.

Let us briefly discuss the generation of magnetosonic waves following Horne et al. (2000) and Chen et al. (2010). The instability is expected to be caused by the *proton ring distribution* (e.g., Thomsen et al. 2017, and references therein) with a positive slope perpendicular to the magnetic field around 10 keV (Fig. 5.15). In the linear regime the growth rate is proportional to the sum of all harmonic resonant interactions between the wave and the protons

$$\omega_i \propto \sum_n \int_0^\infty \left(J_n^2(x) \frac{\partial f(v_\parallel, v_\perp)}{\partial v_\perp} \right) \Big|_{v_\parallel = v_{\parallel res}} \mathrm{d}v_\perp \,, \tag{5.22}$$

where $J_n(x)$ are the Bessel functions of order n, $x = k_\perp v_\perp / \omega_{cp}$, and $f(v_\parallel, v_\perp)$ is the proton distribution function (for a detailed calculation, see Chen et al. 2010). The integral is evaluated at the resonant velocity $v_{\parallel res}$ given by

$$v_{\parallel res} = \frac{\omega}{k_\parallel} \left(1 - \frac{n\omega_{cp}}{\omega} \right) . \tag{5.23}$$

The instability requires that $\partial f / \partial v_\perp > 0$. The positive gradient maximizes when $v_\parallel$ is small because f decreases with increasing $v_\parallel$. The corresponding

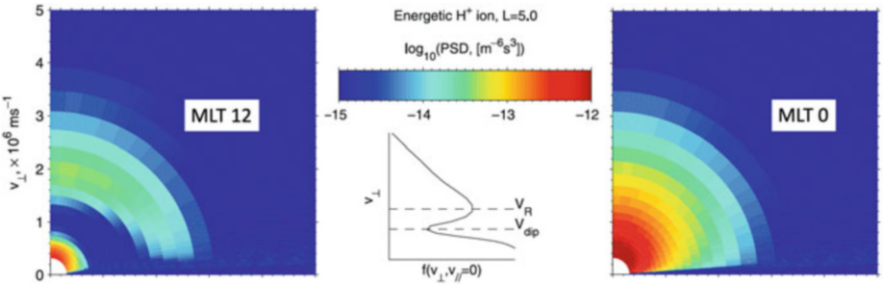

Fig. 5.15 Proton ring distribution. The velocity scales on all axes are the same as on the left vertical axis. The gradient ($\partial f/\partial v_\perp$) of the phase space density of the ring is positive on the dayside (on the left and in the middle), whereas on the nightside (right) the gradient is positive only at the edge of the atmospheric loss cone (From Chen et al. 2010, reprinted by permission from American Geophysical Union)

perpendicular velocity is called the *ring velocity*. Magnetosonic waves have very small $k_\parallel$ and, in order to have small enough resonant velocities, dominant resonances occur at high multiples of proton gyrofrequency $\omega \approx n\omega_{cp}$.

With increasing $k_\perp$ the magnetosonic mode approaches the lower hybrid resonance frequency where $\omega/k_\perp$ decreases. The effective growth of the magnetosonic wave further requires that the Bessel function J_n maximizes in the region where $\partial f/\partial v_\perp$ is positive. The argument of J_n can be written as

$$x = \frac{\omega}{\omega_{cp}} \frac{v_\perp}{v_A}, \tag{5.24}$$

where v_A is the local Alfvén velocity. At high harmonics ($n \gtrsim 10$) J_n maximizes when $x \approx n$ corresponding to the perpendicular velocity close to the Alfvén velocity. If the ring velocity is larger than v_A, the wave can grow. For smaller n the Bessel function peaks instead in a region where $\partial f/\partial v_\perp < 0$ and the wave is damped. For a growing solution at smaller harmonics the ring velocity must exceed the Alfvén velocity with a larger margin. An important factor controlling the growth of the magnetosonic wave is thus the ratio of the ring velocity to the Alfvén velocity.

The energetic proton phase space densities shown in Fig. 5.15 are simulation results of the main phase of the geomagnetic storm on 22 April 2001 calculated at $L = 5$. On the nightside (right) the distribution is bi-Maxwellian with a loss cone. On the dayside (left) the distribution illustrates a ring with a clear peak at about 20 keV. A schematic of typical ring-like phase space density as a function of the perpendicular velocity, indicating velocities at which the phase space density peaks (the ring velocity) and has a minimum (dip velocity), is shown in the middle.

The formation of ion ring distribution can be understood as follows: Lower-energy protons in the nightside plasma sheet E×B drift as shown in Fig. 2.3. Higher-energy protons ($\gtrsim$ 10 keV) are affected by the gradient and curvature effects and drift from the tail predominantly around the dusk toward the dayside. The

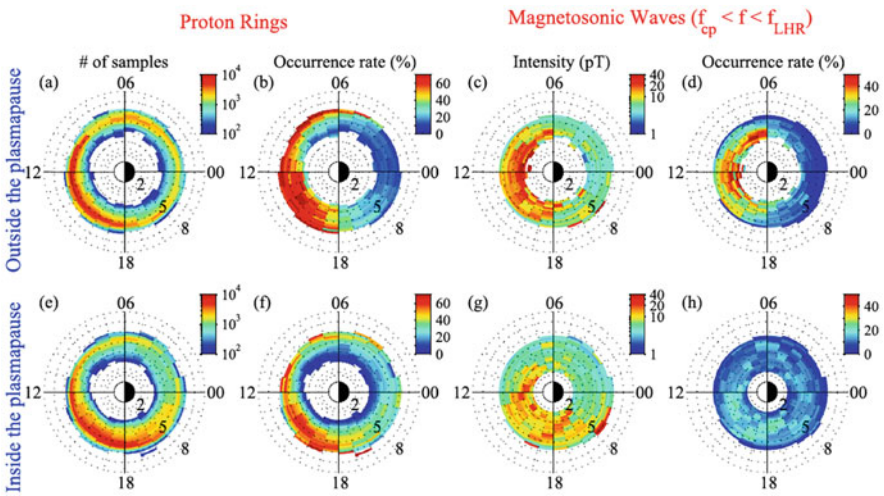

Fig. 5.16 Global distribution of occurrence of proton rings, and occurrence and intensity of magnetosonic waves inside and outside the plasmasphere over 3 years of Van Allen Probes observations. (From Kim and Shprits 2018, reprinted by permission from American Geophysical Union)

gradient and curvature drift rates are proportional to the proton energy, enhancing at dusk and noon the phase space density of higher-energy protons compared to lower energies. In addition, lower-energy protons are subject to charge exchange collisions with exospheric neutrals depleting the core of the proton distribution. The sketch in the middle of Fig. 5.15 demonstrates that below the ring velocity $\partial f/\partial v_{\perp}$ is positive. Thus there is free energy available for the excitation of magnetosonic waves. The negative gradients above the ring velocity and below the velocity at the trough of the distribution function can contribute to the damping of the waves. The natural place for the generation of magnetosonic waves is thus close to the magnetic equator where pitch angles are close to 90° and thus $v_{\parallel}$ is small to maximize the positive gradient of f.

Figure 5.16 shows global spatial distributions of the occurrence of proton rings, and the occurrence and intensity (wave amplitude) of magnetosonic waves inside and outside the plasmapause in *Van Allen Probes* observations. Proton rings and magnetosonic waves are observed over a relatively wide L-range throughout the dayside magnetosphere, both in and outside the plasmasphere. The occurrence of rings and most intense waves is strongest and the L-coverage widest from noon to dusk hours. An exception is outside the plasmasphere in the pre-noon sector at low L-values. The waves are likely generated outside the plasmapause, since in the plasmasphere the Alfvén velocity is well below the ring velocity.

5.4 Drivers of ULF Pc4–Pc5 Waves

While the microscopic instabilities driving whistler-mode, EMIC, and X-mode waves can often be attributed to specific properties of the particle distribution functions, the question of driving ULF waves in the Pc4–Pc5 range is more complicated.

5.4.1 External and Internal Drivers

Magnetospheric ULF waves can be generated both externally by solar wind–magnetopause interactions and internally inside the magnetosphere over a wide range of frequencies. The frequencies of Pc5 oscillations correspond to the longest wavelengths that can be described as propagating or standing waves in the quasi-dipolar domain of the inner magnetosphere. Excitation mechanisms affect the polarization, azimuthal mode number (m), amplitude and frequency of the ULF waves. Azimuthally large-scale (small m) waves are thought to arise primarily from external sources, while azimuthally smaller-scale (large m) waves are more likely excited by internal mechanisms. This division does, however, not always apply (e.g., James et al. 2016, and references therein).

A thorough discussion of external drivers is beyond the scope of this book (for a review, see Hwang and Sibeck 2016, and the extensive set of references therein). In fact, many different perturbations in the upstream solar wind and in the magnetosheath can shake the magnetospheric magnetic field leading to propagating or standing ULF oscillations in the magnetosphere. Obvious candidates are solar wind pressure pulses hitting the magnetopause, the Kelvin–Helmholtz instability (KHI) caused by large enough velocity shear across the magnetopause at the flanks of the magnetosphere (Chen and Hasegawa 1974), and Flux Transfer Events (FTE) through the dayside magnetopause (Russell and Elphic 1979). Furthermore, the magnetosheath and the foreshock region upstream of the magnetosheath host several plasma instabilities from ion gyro-scale kinetic to large-scale mirror-mode instabilities, which may lead to waves penetrating to the magnetosphere.

Correlating different solar wind perturbations with magnetospheric fluctuations is obscured by the interdependence between upstream parameters (e.g., Bentley et al. 2018). Moreover, the dayside magnetopause acts as a low-pass filter suppressing large-amplitude transient pressure pulses in the magnetosheath in timescales shorter a few minutes (Archer et al. 2013). Thus several different effects can result in similar toroidal, poloidal, or compressional ULF waves launched from the magnetopause inward (Fig. 5.17).

A basic scenario of how a perturbation proceeds from the dayside magnetopause inward, is sketched in Fig. 5.18. The inward propagating fast compressional magnetosonic wave launched by an upstream solar wind perturbation encounters increasing Alfvén speed. When the frequency of the wave matches the eigenfrequency

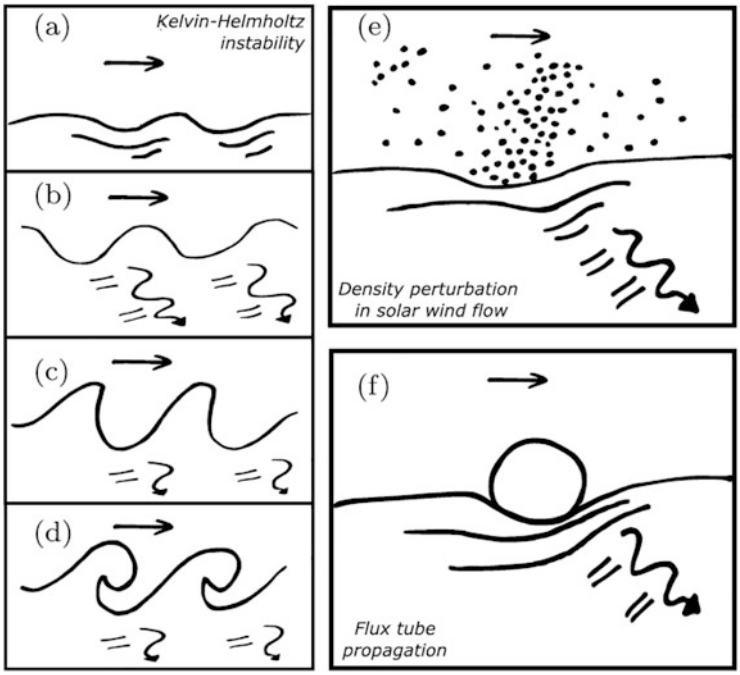

Fig. 5.17 A sketch of different mechanisms on the magnetopause that can drive global magnetospheric ULF oscillations in the Pc4–Pc5 range. Panels (**a**)–(**d**) illustrate the deepening of Kelvin–Helmholtz surface waves to nonlinear vortices, panel (**e**) a solar wind pressure pulse and (**f**) a flux tube pressing the magnetopause (From Bentley et al. 2018, reprinted by permission from American Geophysical Union)

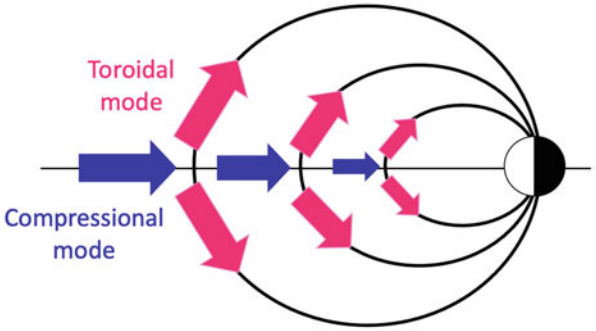

Fig. 5.18 A sketch of the coupling of a fast compressional magnetosonic wave launched at the dayside magnetopause to a toroidal shear Alfvén wave forming field line resonances

$f = nv_A/(2l)$ (Eq. 4.108) of the field line, the wave couples to a toroidal-mode shear Alfvén wave. This leads to a field line resonance (FLR) in the wave guide with reflecting boundaries in the northern and southern ionospheres (Sect. 4.4.2). As the length of the field line (l) is proportional to L, the eigenfrequencies increase with decreasing L-shells. When the compressional mode feeds the toroidal oscillation it gets gradually damped. A similar scenario also applies to the dawn and dusk sectors where the initial perturbation is more likely due to KHI, which may also drive the toroidal mode directly.

The solar wind perturbations can also result in cavity mode oscillations (CMO) of compressional waves in the radial direction (Sect. 4.4.2), although the eigenfrequencies of the cavity modes and their harmonics are rather in the Pc3–Pc4 frequency range than at Pc5 frequencies (e.g., Takahashi et al. 2018).

The largest amplitude ULF waves are associated with the strongest interplanetary shocks (e.g., Hao et al. 2014). The waves can occur over a wide range of L-shells and frequencies and thus affect radiation belt electrons of various energies. The shock-induced ULF waves, however, are quickly damped, most likely via Landau damping with ions of energies of a few keV (e.g., Wang et al. 2015).

Solar wind dynamic pressure oscillations can also directly drive oscillations in the Earth's magnetosphere. The magnetopause responds by contracting and relaxing which leads to compressional magnetic field oscillations in the magnetosphere. This scenario is supported by correlations between fluctuation power in the ULF Pc5 range in the solar wind density/dynamic pressure and in magnetospheric magnetic field found in several experimental studies as well as in simulations showing FLRs when the frequency of solar wind dynamic pressure oscillations matches the local eigenfrequency of the geomagnetic field line (e.g., Claudepierre et al. 2010). If the period of the upstream oscillation is longer than the Alfvén wave travel time through the inner magnetosphere (about 3 min) and the time it takes for a pressure disturbance to propagate past Earth (about 5 min), the perturbation inside the magnetosphere is quasi-static resulting in a phenomenon called *forced breathing of the magnetosphere* (Kepko and Viall 2019).

Internally driven Pc5 waves are commonly ascribed to instabilities due to westward drifting ring current ions and ions injected by substorm dipolarizations or bursty bulk flows from the magnetotail. A possible instability mechanism is the *bounce–drift resonance* between the ions and the ULF wave mode

$$\omega - l\omega_{bi} - m\omega_{di} = 0\,, \tag{5.25}$$

where ω_{bi} and ω_{di} are the bounce and drift frequencies of the ions, l the longitudinal and m the azimuthal mode number of the wave (Southwood et al. 1969).[2]

[2] In Chap. 6 we discuss the bounce and drift resonances in the context of electron diffusion and transport.

Note that the suprathermal ion populations that drive Pc5 waves are the same ions as those driving EMIC waves and may have substantial anisotropies ($T_\perp > T_\parallel$ or $P_\perp > P_\parallel$), being capable to drive mirror mode waves with magnetic field and density oscillations in opposite phases to each other (Sect. 4.4.1). The threshold for the mirror mode instability must be calculated from kinetic theory resulting in

$$\sum_\alpha \frac{\beta_{\alpha\perp}^2}{\beta_{\alpha\parallel}} > 1 + \sum_\alpha \beta_{\alpha\perp} \,. \tag{5.26}$$

where β_α are the beta parameters, i.e., the ratios of the plasma and magnetic pressures, for each plasma species. Chen and Hasegawa (1991) conducted a theoretical kinetic treatment in realistic magnetospheric plasma conditions assuming a core ($\sim$ 100 eV) and energetic ($\sim$ 10 keV) components and concluded that mirror instability is an important internal mechanism to drive ULF waves. Consequently, the local instability can support a slow mode ULF oscillation against its damping through the Landau mechanism.

Figure 5.19 shows an example of an observed ULF wave event during a weak storm on 6 July 2013 investigated by Xia et al. (2016). At the time indicated by the vertical dashed lines in the figure the *Van Allen Probe* B was in the evening sector (MLT $\approx$ 21:40) at $L \approx 5.5$ close to magnetic equator. At this time there was a clear pressure anisotropy ($P_\perp > P_\parallel$) and the total magnetic field and the plasma density oscillated in opposite phases. As usual the wave had mixed polarization. The parallel

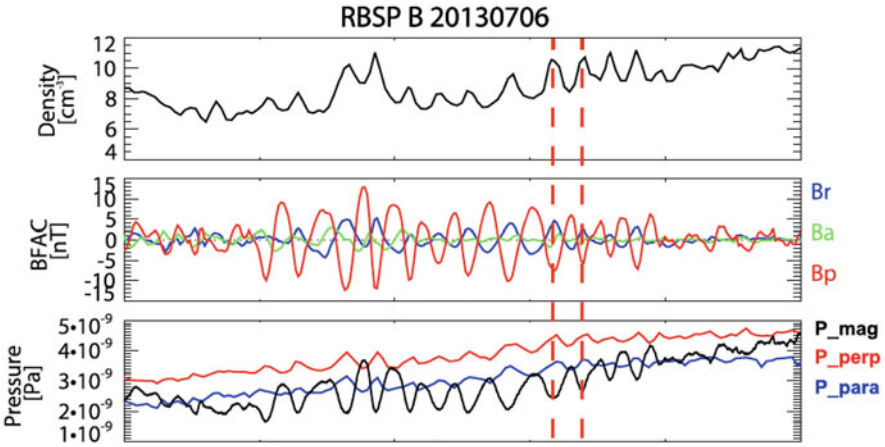

Fig. 5.19 *Van Allen Probe* B observation of a poloidal mode ULF wave with magnetic and density fluctuations in opposite phases. The top panel shows the density fluctuation, the center panel the magnetic field components in field-aligned coordinates (blue: radial, green: azimuthal, red: parallel). In the bottom panel the black line shows the magnetic pressure which is clearly in opposite phase to parallel (blue) and perpendicular (red) plasma pressures. the dashed vertical lines are there to guide the eye (From Xia et al. 2016, reprinted by permission from American Geophysical Union)

(poloidal) component was larger than the radial (compressional) component and the azimuthal component of the waves was smallest. Thus the wave was a dominantly poloidal mode with mirror-mode type compression consistent with the anisotropy-driven drift-mirror instability.

James et al. (2016) investigated substorm-associated ULF waves using observations of the far-ultraviolet imager of the IMAGE satellite, several ground-based magnetometer arrays and the SuperDARN network of coherent ionospheric radars. The advantage of the radars is that they measure large-scale plasma fluctuations in the ionosphere whereas only a fraction of the wave power is transmitted through the ionosphere to ground. In the three events studied in detail by James et al. (2016) the properties of the waves varied widely both within and between the events, being different at different distances from the ionospheric location of the substorm. The waves were found to be poloidal modes with azimuthal wave numbers from -9 to -44, indicating that the phase of the waves propagated westward, which is consistent with westward drifting protons as wave drivers in the magnetosphere. The energies of the protons were estimated from the resonance condition to be in the range 2–66 keV.

The determination of the azimuthal mode number from spacecraft observations is notoriously difficult. The measurements need to be performed at the same L-shell by at least two spacecraft close enough to each other in order to avoid the 2π ambiguity (aliasing) in the calculation of the phase difference between the observed oscillations. Murphy et al. (2018) performed a detailed analysis of ULF Pc4–Pc5 wave observations of the closely-spaced MMS spacecraft during a period of solar wind high-speed stream between 25 September and 10 October 2016. Due to the highly-elliptical orbit the velocity of the satellites close to the perigee of the constellation ($1.2\,R_E$) was so high that the analysis was limited outside $4\,R_E$ but reaching up to the magnetopause in the evening sector where the apogee was at the time of the observations. The ULF wave power peaked close to the magnetopause and in the inner magnetosphere at equatorial distances 6–8 R_E.

Murphy et al. (2018) calculated the azimuthal mode numbers for discrete ULF waves observed during the investigated period. The distribution of m at distances 4–14 R_E is shown in Fig. 5.20. The mode numbers were found to be both positive (indicating eastward propagation of the wave) and negative (indicating westward propagation of the wave) reaching up to ± 100 but preferentially within $|m| < 20$. At equatorial distances up to $8\,R_E$ the mode numbers were predominantly positive and < 20, between 8 and $11\,R_E$ predominantly between -5 and -40 and close to the magnetopause beyond $13\,R_E$ again mostly positive and < 20. The positive mode numbers were interpreted to indicate an external driver and the negative ones an internal driver. The latter is consistent with the internal driver being protons passing the Earth on the evening side and driving westward propagating ULF waves similarly to the above mentioned results of James et al. (2016).

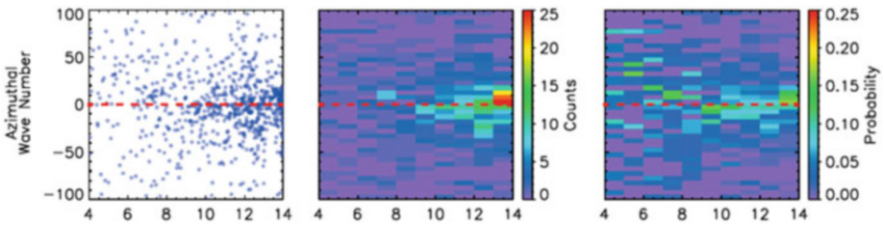

Fig. 5.20 Left: the distribution of azimuthal mode numbers; middle: the histogram of the distribution; right: the probability distribution. The horizontal axis is the Earth-centered distance in R_E (From Murphy et al. 2018, Creative Commons Attribution License)

5.4.2 Spatial Distribution of ULF Waves

The wide spatial range of ULF oscillations from the magnetopause to the ionosphere and the great variability of the wave properties under different solar wind conditions and magnetospheric activity pose challenges to the production of comprehensive maps of the distribution of the waves. Furthermore, a reliable determination of the polarization requires simultaneous observation of a sufficient number of electric and magnetic field components, preferentially all of them. Measuring the magnetic field components often is sufficient, but the polarization of the electric field is needed, in particular, close to the equator where the magnetic field of the fundamental ($n = 1$) FLR has a node yielding a weak magnetic field signature in the observation. Consequently, different studies based on different satellite and ground-based observations have led to different, sometimes contradictory, conclusions.

Hudson et al. (2004a) investigated ULF oscillations in the range $L = 4 - 9$ over 14 months of CRRES observations, which took place close to the maximum of Solar Cycle 22. Toroidal Pc5 oscillations were found on the dusk and dawn flanks of the magnetosphere inside $L = 8$, preferentially at the higher end of the L-shells. Based on the observed local plasma frequency the waves were found to be standing FLRs at the fundamental frequency $f = v_A/(2l)$. Poloidal (including compressional) modes were found to occur in the dusk-to-midnight sector mostly from $L = 5$ to $L = 8$. This is consistent with above discussed instability driven by ions injected from the magnetotail. The orbit of CRRES did not allow sufficient sampling on the dayside and thus the important dayside compressional modes were not covered in the study.

The most comprehensive picture of Pc4–Pc5 oscillations has been obtained from the THEMIS mission. As already illustrated in Fig. 4.7, the magnetometer and the electric field instrument of THEMIS have made possible a complete characterization of different polarization components. Furthermore, after October 2007 the orbital configuration of the spacecraft allowed a full nearly-equatorial coverage of all local times in 13 months reaching out to about 10 R_E.

Liu et al. (2009) performed a statistical study of Pc4–Pc5 events observed from November 2007 to December 2008. The total observation time was more than 3000 h. Of the identified wave events 9805 were in the Pc4 range and 50,184 in

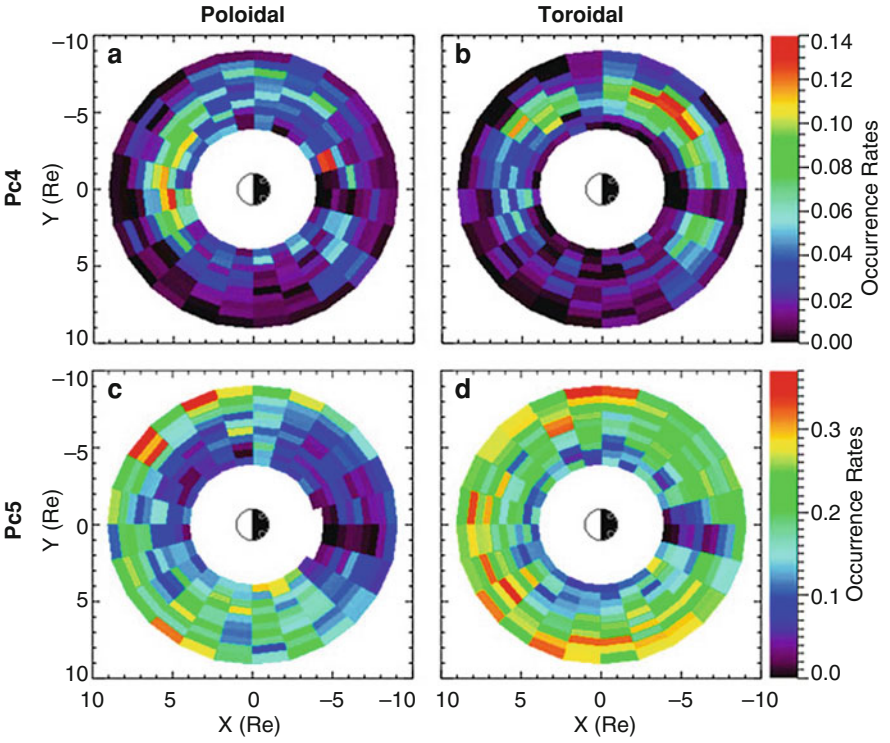

Fig. 5.21 Spatial distribution of the occurrence rates of poloidal and toroidal ULF Pc4 and Pc5 events. The bins are 0.5 R_E wide in the radial direction from 4 to 9 R_E and 15 min in the local time. (From Liu et al. 2009, reprinted by permission from American Geophysical Union)

the Pc5 range. In both frequency ranges the number of toroidal events was a little larger than the number of poloidal events (Pc4: 51%, Pc5: 59%).

The spatial distribution of the occurrence rates of poloidal (including the compressional) and toroidal modes are shown in Fig. 5.21. Pc4 events were most frequent at radial distances 5–6 R_E form the post-midnight (mostly toroidal) to noon (mostly poloidal), whereas Pc5 events were most frequent at distances 7–9 R_E. That poloidal events occur mostly on the dayside is consistent with upstream solar wind perturbations. The enhancement of poloidal Pc5 events on the dusk flank is, in turn, consistent with the internal driving through bounce–drift resonance with ring current ions and/or ions freshly injected from the tail.

The different radial distributions of the toroidal Pc4 and Pc5 modes are likely related to the inverse dependence of the FLR frequency on the length of the field line. The high occurrence rates of toroidal Pc5 events close to the dawn and dusk sectors is an indication that the waves may be driven directly by the Kelvin–Helmholtz instability on the flanks of the magnetosphere. Liu et al. (2009) suggested that the relatively low occurrence rates of both poloidal and toroidal Pc4 events in

the dusk sector would be due to the extension of the plasmapause further out during low magnetospheric activity.

Liu et al. (2009) also investigated the distribution of wave power. Overall the wave power was higher in the Pc5 than the Pc4 band. In both frequency bands the power decreased with decreasing radial distance from the Earth.